A&A 385, 337–364 (2002)
DOI: 10.1051/0004-6361:20011817

Astronomy
&
Astrophysics

Cosmological hydrodynamics with adaptive mesh refinement

A new high resolution code called RAMSES

R. Teyssier*

Commissariat à l'Énergie Atomique, Direction des Sciences de la Matière, Service d'Astrophysique,
Centre d'Études de Saclay, L'orme des Merisiers, 91191 Gif-sur-Yvette Cedex, France
and
Numerical Investigations in Cosmology (NIC group), CEA Saclay, France

Received 18 June 2001 / Accepted 12 December 2001

Abstract. A new N-body and hydrodynamical code, called RAMSES, is presented. It has been designed to study structure formation in the universe with high spatial resolution. The code is based on Adaptive Mesh Refinement (AMR) technique, with a tree-based data structure allowing recursive grid refinements on a cell-by-cell basis. The N-body solver is very similar to the one developed for the ART code (Kravtsov et al. 1997), with minor differences in the exact implementation. The hydrodynamical solver is based on a second-order Godunov method, a modern shock-capturing scheme known to compute accurately the thermal history of the fluid component. The accuracy of the code is carefully estimated using various test cases, from pure gas dynamical tests to cosmological ones. The specific refinement strategy used in cosmological simulations is described, and potential spurious effects associated with shock waves propagation in the resulting AMR grid are discussed and found to be negligible. Results obtained in a large N-body and hydrodynamical simulation of structure formation in a low density ΛCDM universe are reported, with 256^3 particles and 4.1×10^7 cells in the AMR grid, reaching a formal resolution of 8192^3. A convergence analysis of different quantities, such as dark matter density power spectrum, gas pressure power spectrum and individual haloe temperature profiles, shows that numerical results are converging down to the actual resolution limit of the code, and are well reproduced by recent analytical predictions in the framework of the halo model.

Key words. gravitation – hydrodynamics – methods: numerical – cosmology: theory – cosmology: large-scale structure of Universe

1. Introduction

Numerical simulations of structure formation in the universe are now widely used to understand the highly nonlinear nature of gravitational clustering. Dark matter is believed to be the dominant component in the mass of the cosmological density field, with only a small fraction (say 10%) in baryons. At intermediate scales, such as galaxy clusters, dark matter still dominates the total gravitational mass, but the introduction of a gaseous component appears to be unavoidable, since X-ray or Sunyaev-Zeldovich observations of the hot intracluster medium give us strong constraints on the structure of galaxy clusters. On smaller scales, gas cooling and fluid dynamics play a dominant role in the structure of galaxy-size object. Although baryons can be described to first order as a hydrostatic ionized plasma trapped in dark matter potential wells, the complexity of hydrodynamical processes such as shock heating, atomic radiation cooling and, ultimately, star formation requires an accurate treatment of the baryonic component.

For a cosmological simulation to be realistic, high mass and spatial resolution are needed. While the former is related to the initial number of degrees of freedom (usually "particles" or "wavelengths") in the computational volume, the latter is usually related to the numerical method specifically used to compute the particles trajectory. For a $\Omega = 1$ universe, using a sufficiently large volume of, say, 100 Mpc h^{-1} aside, we need at least 256^3 particles to describe $L_\star$ galaxies with 100 particles. In order to resolve the internal radial structure of such haloes with at least 10 resolution elements, we need a spatial resolution of 10 kpc h^{-1} or equivalently a dynamical range of 10^4.

The Particle-Mesh method (Hockney & Eastwood 1981; Klypin & Shandarin 1983) is perhaps the simplest and fastest N-body algorithm for solving gravitational dynamics, but it is limited by computer resources to a dynamical range of 10^3. The P3M method (Hockney & Eastwood 1981; Efstathiou et al. 1985) can reach a higher spatial resolution, by adding a small scale component to the PM force, directly computed from the two-body interactions ("Particle-Particle") between neighboring particles. This method suffers however from a dramatic increase

---

* e-mail: `Romain.Teyssier@cea.fr`

in CPU time as clustering develops and as short range forces become dominant. An improvement of this method was therefore developed for the AP3M code (Couchman 1991): a hierarchy of recursively refined rectangular grids is placed in clustered regions where a local PM solver is activated to speed up the PP calculations. Another N-body method which can achieve high dynamical range is the TREE code (Barnes & Hut 1986; Bouchet & Hernquist 1988), which properly sort neighboring particles in a recursive tree structure. Long-range interactions are computed using multipole expansion and low resolution nodes of the tree, while short range interactions are computed using a PP approach between particles belonging to the same leaf of the tree.

The idea of using Adaptive Mesh Refinement (AMR) for N-body methods appears as a natural generalization of both AP3M and TREE codes, since they use a hierarchy of nested grids to increase the spatial resolution locally. The recently developed ART code (Kravtsov et al. 1997) offers, in this respect, the first implementation of a grid-based high-resolution N-body code, where the mesh is defined on a recursively refined spatial tree. ART takes advantage of both the speed of a mesh-based Poisson solvers and the high-dynamical range and flexibility obtained with a tree structure. Since no PP force is considered in the ART method, the resolution is not uniform (as opposed to AP3M and TREE codes), but proportional to the local cell size of the grid. The grid is continuously refined or de-refined in the course of the simulation, to ensure that the mean number of particles par cell remains roughly constant (around 10). This "quasi-Lagrangian" approach ensures that two-body relaxation remains unimportant (Knebe et al. 2000).

The gaseous component, baryons, can be described using one of several hydrodynamical methods widely used today in cosmology. They can be divided into three groups: Lagrangian schemes, Eulerian schemes and intermediate schemes.

1- Lagrangian schemes or quasi-Lagrangian schemes (Gnedin 1995; Pen 1995) are based on a moving mesh that closely follows the geometry of the flow for a constant number of grid points. The grid adapts itself to collapsing fluid elements, but suffers from severe mesh distortion in the non linear stage of gravitational clustering (Gnedin & Bertschinger 1996). The coupling with one of the aformentioned N-body solvers is also non-trivial (ibid).

2- Eulerian schemes are usually based on a uniform Cartesian mesh, which make them suitable for a coupling with the traditional, low-resolution PM solver (Cen 1992; Ryu et al. 1993; Teyssier et al. 1998; Chieze et al. 1998). They suffer however from limited dynamic range.

3- Smooth Particles Hydrodynamics (SPH) can be thought as an intermediate solution. This is a particle-based method, which follows the Lagrangian evolution of the flow, but in which resolution elements are defined as appropriate averages over 50 neighboring particles (Gingold & Monaghan 1977; Evrard 1988; Hernquist & Katz 1989). This "smoothing kernel" defines the effective Eulerian resolution of the method. The SPH method offers also the possibility of a straightforward coupling to particle-based N-body solver like the AP3M or TREE codes. The main drawback of the SPH method is its relative poor discontinuity capturing capabilities (one needs at least 50 particles per resolution element in order to properly describe sharp features, like shock waves or contact surfaces) and the fact that it relies on the artificial viscosity method to capture shock waves.

One of the most promising hydrodynamical methods at this time is the AMR scheme, described originally in Berger & Oliger (1984) and Berger & Collela (1989). The original AMR method is an Eulerian hydrodynamics scheme, with a hierarchy of nested grids covering high-resolution regions of the flow. The building blocks of the computational grid are therefore rectangular patches of various sizes, whose positions and aspects ratio are optimized with respect to flow geometry, speed and memory constraints. Let's call this spatial structure "patch-based AMR". An alternative method was proposed by several authors (see Khokhlov 1998, and reference therein) where parent cells are refined into children cells, on a cell-by-cell basis. As opposed to the original patch-based AMR, let us call this last method "tree-based AMR", since the natural data structure associated to this scheme is a recursive tree structure. The resulting grid follows complex flow geometry more closely, at the price of a data management which is more complicated than patch-based AMR. These two different adaptive mesh structures can be coupled to any grid-based fluid dynamics scheme. It is worth mentioning that modern high-resolution shock capturing methods are all grid-based and have number of interesting features: they are stable up to large Courant numbers, they are striclty conservative for the Euler equations and they are able to capture discontinuities within only few cells. Among several schemes, higher order Godunov methods appear to be more accurate and to be easy to generalize in 3 dimensions.

The original patch-based AMR, based on the Piecewise Parabolic Method (PPM: a third-order Godunov scheme), was recently adapted to cosmology (Bryan & Norman 1997; Abel et al. 2000). The hydrodynamical scheme was coupled to the AP3M N-body solver (without using the PP interaction module). This choice is natural since both codes use a set of rectangular patches to cover high-resolution regions of the flow.

In this paper, an alternative solution is explored: coupling a tree-based AMR hydrodynamical scheme to the N-body solver developed for the ART code (Kravtsov et al. 1997). This solution seems indeed more suitable for the hierarchical clustering picture where a very complex geometry builds up, with a large number of small clumps merging progressively to form large virialized haloes and filaments. The number of grids required to cover efficiently all these small haloes is so large, that it renders a patch-based approach less efficient.

In this paper, a newly developed N-body and hydrodynamical code, called RAMSES, is presented. It is a tree-based AMR using the "Fully Threaded Tree" data structure of Khokhlov (1998). The N-body solver is largely inspired by the ART code (Kravtsov et al. 1997), with some differences in the final implementation. The hydrodynamical solver is a second-order Godunov scheme for perfect gases (also called Piecewise Linear Method or PLM). In Sect. 2, the N-body and hydrodynamical algorithms developed for RAMSES are briefly described, with emphasis put on the original solutions discovered in the course of this work. In Sect. 3, results obtained by RAMSES for standard test cases are presented, demonstrating the accuracy of the method. Pure hydrodynamical problems are considered first, showing that shocks and contact surfaces are well captured by the tree-based AMR scheme.

Great care is taken to demonstrate that refining the mesh in shock fronts can be avoided in cosmological contexts. Indeed, potentially spurious effects associated to the AMR grid remains low enough to apply the method safely using refinements in high density regions only. In Sect. 4, results of a large cosmological simulation using 256^3 particles, with coupled gas and dark matter dynamics, are reported and compared to various analytical predictions. In Sect. 5, the results presented in this paper are summarized, and future projects are discussed.

2. Numerical methods

The modules used in RAMSES can be divided into 4 parts: the AMR service routines, the Particle Mesh routines, the Poisson solver routines and the hydrodynamical routines. The dimensionality, noted dim, can be anything among 1, 2 or 3.

2.1. Adaptive mesh refinement

The fundamental data structure in RAMSES is called a "Fully Threaded Tree" (FTT) (Khokhlov 1998). Basic elements are not single cells, but rather groups of $2^{\rm dim}$ sibling cells called *octs*. Each oct belongs to a given level of refinement labeled ℓ. A regular Cartesian grid, called the coarse grid, defines the base of the tree structure ($\ell = 0$). In order to access all octs of a given level, octs are sorted in a double linked list. Each oct at level ℓ points to the previous and the next oct in the level linked list, but also to the parent cell at level $\ell - 1$, to the $2 \times {\rm dim}$ neighboring parent cells at level $\ell - 1$ and to the $2^{\rm dim}$ child octs at level $\ell + 1$. If a cell has no children, it is called a *leaf* cell, and the pointer to the child oct is set to *null*. Otherwise, the cell is called a *split cell*. In order to store this particular tree structure in memory, one needs therefore 17 integers per oct for dim = 3, or equivalently 2.125 integers per cell.

In RAMSES, time integration can be perfomed in principle for each level independantly. Only two time stepping algorithms have been implemented so far: a single time step scheme and an adaptive time step scheme. The single time step algorithm consists in integrating the equations from t to $t + \Delta t$, with the same time step Δt for all levels. The adaptive time step algorithm, on the other hand, is similar to a "W cycle" in the multigrid terminology. Each level is evolved in time with its own time step, determined by a level dependant CFL stability condition. Consequenty, when level $\ell = 0$ is advanced in time using one coarse time step, level $\ell = 1$ is advanced in time using two time steps, level $\ell = 2$ using 4 time steps, and so on. An additional constraint on these level dependant time steps comes from synchronization, namely $\Delta t_\ell = \Delta t^1_{\ell+1} + \Delta t^2_{\ell+1}$.

Within one time step and for each level, each operation is perfomed in the following way: a sub-sample of octs is first gathered from the tree. Gathered cells can then be modified very efficiently on vector or parallel architectures. Finally, updated quantities are scattered back to the tree. When one needs to access neighboring cells (in order to compute gradients for example), it is straightforward to obtain the neighboring oct addresses from the tree, and then to compute the neighboring cell addresses.

The two main routines used to dynamically modify the AMR structure at each time step are now described.

2.1.1. Building the refinement map

The first step consists of marking cells for refinement according to *user-defined* refinement criteria, within the constraint given by a strict refinement rule: any oct in the tree structure has to be surrounded by $3^{\rm dim} - 1$ neighboring parent cells. Thanks to this rule, a smooth transition in spatial resolution between levels is enforced, even in the diagonal directions. Practically, this step consists in three passes through each level, starting from the finer level $\ell_{\rm max}$ down to the coarse grid $\ell = 0$.

1. If a split cell contains a children cell that is marked or already refined, then mark it for refinement;
2. Mark the $3^{\rm dim} - 1$ neighboring cells;
3. If any cell satisfies the user-defined refinement criteria, then mark it for refinement.

One key ingredient still missing in this procedure is the so-called "mesh smoothing". Usually, refinement are activated when gradients (or second derivatives) in the flow variables exceed a given threshold. The resulting refinement map tends to be "noisy", especially in smooth part of the flow where gradients fluctuates around the threshold. Khokhlov (1998) describes a very sophisticated method based on a reaction-diffusion operator applied on the refinement map. I prefer to use here the simpler approach of Kravtsov et al. (1997) in the ART code, where a cubic buffer is expanded *several times* around marked cells. The number of times one applies the smoothing operator on the refinement map is obviously a free parameter. This parameter is noted $n_{\rm expand}$. In the ART code, this operator is applied twice at each time step. In RAMSES, it is usually applied only once, since, as we see below, boundary conditions are defined for each level in a slightly more sophisticated way than in ART, using *buffer regions* (see

Sect. 2.2.3). Therefore, the extra mesh smoothing used in ART can be thought as a way of creating the equivalent of the buffer regions in RAMSES.

Note that the exact method implemented here and in the ART code leads to a convex structure for the resulting mesh, that is likely to increase the overall stability of the algorithm. Note also that only refinement criteria are necessary in RAMSES: no *de-refinement* criteria need to be specified by the user. This is an important difference compared to other approaches (Kravtsov et al. 1997; Khokhlov 1998).

2.1.2. Modifying the tree structure

The next step consists in splitting or destroying children cells according to the refinement map. RAMSES performs two passes through each level, starting from the coarse grid $\ell = 0$, up to the finer grid $\ell_{\max}$:

1. If a leaf cell is marked for refinement, then create its child oct;
2. If a split cell is not marked for refinement, then destroy its child oct.

Creating or destroying a child oct is a time-consuming step, since it implies reorganizing the tree structure. Thanks to the double linked list associated to the FTT tree structure, this is done very efficiently by first disconnecting the child oct from the list, and then reconnecting the list in between the previous and next octs. Note however that this operation can not be vectorized. It is important to stress that this operation is applied at each time step, but *for a very small number of octs*. In other word, at each time step, the mesh structure is not rebuilt from scratch, but it is slightly modified, in order to follow the evolution of the flow. Since the refinement map has been carefully built during the last step, the refinement rule should be satisfied by construction. This is however not the case if one uses the adaptive time step method described in Sect. 2.3.2. In this case, a final check is performed before splitting leaf cells. If the refinement rule is about to be violated, leaf cells are not refined.

2.2. N-body solver

The N-body scheme used in RAMSES is similar in many aspects to the ART code of Kravtsov et al. (1997). Since the ART code was not publicily available at the time this work was initiated, a new code had to be implemented from scratch. I briefly recall here the main ingredients of the method, outlining the differences between the two implementations.

A collisionless N-body system is described by the Vlasov-Poisson equations, which, in terms of particles (labeled by "p"), reads

$$\frac{\mathrm{d}\boldsymbol{x}_{\mathrm{p}}}{\mathrm{d}t} = \boldsymbol{v}_{\mathrm{p}} \text{ and } \frac{\mathrm{d}\boldsymbol{v}_{\mathrm{p}}}{\mathrm{d}t} = -\nabla_x \phi \text{ where } \triangle_x \phi = 4\pi G \rho. \quad (1)$$

Grid-based N-body schemes, such as the standard PM, are usually decomposed in the following steps:

1. Compute the mass density ρ on the mesh using a "Cloud-In-Cell" (CIC) interpolation scheme;
2. Solve for the potential ϕ on the mesh using the Poisson equation;
3. Compute the acceleration on the mesh using a standard finite-difference approximation of the gradient;
4. Compute each particle acceleration using an inverse CIC interpolation scheme;
5. Update each particle velocity according to its acceleration;
6. Update each particle position according to its velocity.

The specific constraints of a tree-based AMR N-body solver are now discussed in more details.

2.2.1. The particle linked list

Since we are dealing with an AMR grid, we need to know which particle is interacting with a given cell. This is done thanks to a particle linked list. Particles belong to a given oct, if their position fits exactly into the oct boundaries. All particles belonging to the same oct are linked together. In order to build this linked list, we have to store the position of each oct in the tree structure. Moreover, each oct needs to have access to the address of the first particle in the list and to the total number of particles contained in its boundaries. We need therefore to store these two new integers in the FTT tree structure.

The particle linked list is built in a way similar to the TREE code: particles are first divided among the octs sitting at the coarse level $\ell = 0$. Each individual linked list is then recursively divided among the children octs, up to the finer level $\ell = \ell_{\max}$. Going from level ℓ to level $\ell + 1$ implies removing from the linked list particles sitting within split cell boundaries. Going from level $\ell + 1$ to level ℓ implies reconnecting the children linked lists to the parent one. In the adaptive time step case, in order to avoid rebuilding the whole tree from the coarse level, particle positions are checked against parent octs boundaries and, if necessary, are passed to neighboring octs using the information stored in the FTT tree.

2.2.2. Computing the density field

The density field is computed using the CIC interpolation scheme (Hockney & Eastwood 1981). For each level, particles sitting inside level ℓ boundaries are first considered. This can be done using the level ℓ particle linked list. Particles sitting outside the current level, but whose clouds intersect the corresponding volume are then taken into account. This is done by examining particles sitting inside neighboring parent cells at level $\ell - 1$. Note that in this case the size of the overlapping cloud is the one of level ℓ particles. In this way, for a given set of particle positions, the resulting density field at level ℓ is exactly the same as that of a regular Cartesian mesh of equivalent spatial resolution.

2.2.3. Solving the Poisson equation

Several methods are described in the literature to solve for the Poisson equation in the adaptive grids framework (Couchman 1991; Jessop et al. 1994; Kravtsov et al. 1997; Almgren et al. 1998; Truelove et al. 1998). In RAMSES, as in the ART code, the Poisson equation is solved using a "one-way interface" scheme (Jessop et al. 1994; Kravtsov et al. 1997): the coarse grid solution never "sees" the effect of the fine grids. The resulting accuracy is the same as if the coarse grid were alone. Boundary conditions are passed only from the coarse grid to the fine grid by a linear interpolation. For each AMR level, the solution should therefore be close to the one obtained with a Cartesian mesh of equivalent spatial resolution, but *it can not be better in any way.* A better accuracy would be obtained using a two-way interface scheme, as the one described for example in Truelove et al. (1998). Such a sophisticated improvement of the Poisson solver is left for future work.

The Poisson equation at the coarse level is solved using standard Fast Fourier Transform (FFT) technique (Hockney & Eastwood 1981), with a Green function corresponding to Fourier transform of the 2dim + 1-points finite difference approximation of the Laplacian. For fine levels ($\ell > 0$), the potential is found using a relaxation method similar to the one developed for the ART code: the Poisson equation is solved using the 2dim + 1-points finite difference approximation of the Laplacian, with Dirichlet boundary conditions. In RAMSES, boundary conditions are defined in a temporary buffer region surrounding the level domain, where the potential is computed from level $\ell - 1$ through a linear reconstruction.

Using these specific boundary conditions, the potential can be computed using any efficient relaxation method. In RAMSES, the Gauss-Seidel (GS) method with Red-Black Ordering and Successive Over Relaxation (Press et al. 1992) is used. In two dimensions, for unit mesh spacing, the basic GS writes as

$$\phi_{i,j}^{n+1} = \frac{1}{4}\left(\phi_{i+1,j}^{n} + \phi_{i-1,j}^{n} + \phi_{i,j+1}^{n} + \phi_{i,j-1}^{n}\right) - \frac{1}{4}\rho_{i,j}. \quad (2)$$

This iteration is applied first to update the potential for "black" cells defined by i odd and j odd or i even and j even, and then to update the potential for "red" cells defined by i odd and j even or i even and j odd. Finally, the result is "over-corrected" using the so-called over-relaxation parameter ω

$$\phi_{i,j}^{n+1} = \omega\phi_{i,j}^{n} + (1-\omega)\phi_{i,j}^{n+1} \quad \text{with} \quad 1 < \omega < 2. \quad (3)$$

The speed of the algorithm relies on the correct choice for both ω and the initial guess $\phi_{i,j}^{0}$. For a regular $N \times N$ Cartesian mesh, the optimal over-relaxation parameter is known to be (Press et al. 1992)

$$\omega \simeq \frac{2}{1 + \alpha\frac{\pi}{N}} \quad (4)$$

where $\alpha = 1$ for Dirichlet boundary conditions and $\alpha = 2$ for periodic boundary conditions. For an irregular AMR grid, the situation is more complicated, since the computational volume is covered by irregular mesh patches. The over-relaxation parameter has to be found empirically. An interesting way of determining the optimal value for ω is to estimate the average size $< L >$ of these patches, and to use it in formula (4) in place of N. It was found to work very well in practice.

The initial guess is obtained from the coarser level $\ell - 1$ through a linear reconstruction of the potential. In this way, the solution at large scale is correctly captured at the very beginning of the relaxation process. Only the shortest wavelengths need to be further corrected.

A question that arises naturally is: when do we reach convergence? Since our Poisson solver is coupled to a N-body system, errors due to the CIC interpolation scheme are dominant in the force calculation. As soon as the residuals are smaller than the CIC induced errors, further iterations are unnecessary. For cosmological simulations, this is obtained by specifying that the 2-norm of the residual has to be reduced by a factor of at least 10^3.

Let us consider a 128^3 coarse grid, completely refined in a 256^3 underlying fine grid. Solving first the Poisson equation on the coarse level using FFT, the solution is injected to the fine grid as a first guess. In this particular example, the optimal over-relaxation parameter is $\omega \simeq 1.9$ (using Eq. (4) with $\alpha = 2$) and 60 iterations are needed to damped the errors sufficiently.

Let us now consider a more practical example, in which a typical AMR grid is obtained from a cosmological simulation. In this case, the average AMR patch size was empirically found to be roughly $< L > \simeq 20$ cells. Equation (4) with $\alpha = 1$ gives $\omega \simeq 1.7$. 20 iterations only are needed for the iterative solver to converge sufficiently. Note that for the ART code, the optimal value was found to be $\omega = 1.25$ (Kravtsov et al. 1997), using however a different approach to set up boundary conditions.

2.2.4. Computing the acceleration

Using the potential, the acceleration is computed on the mesh using the 5-points finite difference approximation of the gradient. As for the potential, the acceleration is cell-centered and the gradient stencil is symmetrical in order to avoid self-forces (Hockney & Eastwood 1981). Buffer regions defined during the previous step are used here again to give correct boundary conditions. The acceleration is interpolated back to the particles of the current level, using an inverse CIC scheme. Only particles from the linked list whose cloud is entirely included within the level boundary are concerned. For particles belonging to level ℓ, but whose cloud lies partially outside the level volume, the acceleration is interpolated from the mesh of level $\ell - 1$. This is the same for the ART code: *"In this way, particles are driven by the coarse force until they move sufficiently far into the finer mesh"* (Kravtsov et al. 1997).

2.2.5. Time integration

One requirement in a coupled N-body and hydrodynamical code is the possibility to deal with variable time steps. The stability conditions for the time step is indeed given by the Courant Friedrich Levy (CFL) condition, which can vary in time. The standard leapfrog scheme (Hockney & Eastwood 1981), though accurate, does not offer this possibility. In RAMSES, a second-order midpoint scheme has been implemented, which reduces exactly to the second order leapfrog scheme for constant time steps. Since the acceleration $-\nabla\phi^n$ is known at time t^n from particle positions $\boldsymbol{x}_{\rm p}^n$, positions and velocities are updated first by a predictor step

$$\boldsymbol{v}_{\rm p}^{n+1/2} = \boldsymbol{v}_{\rm p}^n - \nabla\phi^n \Delta t^n/2 \tag{5}$$

$$\boldsymbol{x}_{\rm p}^{n+1} = \boldsymbol{x}_{\rm p}^n + \boldsymbol{v}_{\rm p}^{n+1/2}\Delta t^n \tag{6}$$

and then by a corrector step

$$\boldsymbol{v}_{\rm p}^{n+1} = \boldsymbol{v}_{\rm p}^{n+1/2} - \nabla\phi^{n+1}\Delta t^n/2. \tag{7}$$

In this last equation, the acceleration at time t^{n+1} is needed. In order to avoid an extra call to the Poisson solver, this last operation is postponed to the next time step. The new velocity is computed as soon as the new potential is obtained. In RAMSES, it is possible to have either a single time step for all particles, or individual time steps for each level. In the latter case, when a particle exits level ℓ with time step Δt_ℓ, the corrector step is applied at level $\ell-1$, using Δt_ℓ in place of $\Delta t_{\ell-1}$. Therefore, the "past history" of all particles has to be known in order to apply correctly the corrector step. This is done in RAMSES by introducing one extra integer per particle indicating its current level. This particle "color" is eventually modified at the end of the corrector step.

Usually, the time step evolution is smooth, making our integration scheme second-order in time. However, if one uses the adaptive time step scheme instead of the more accurate (but time consuming) single time step scheme, the time step changes abruptly by a factor of two for particles crossing a refinement boundary. Only first order accuracy is retained along those particle trajectories. This loss of accuracy has been analyzed in realistic cosmological conditions (Kravtsov & Klypin 1999; Yahagi & Yoshii 2001) and turns out to have a small effect on the particle distribution, when compared to the single time step case.

2.3. Hydrodynamical solver

In RAMSES, the Euler equations are solved in their conservative form:

$$\frac{\partial\rho}{\partial t} + \nabla\cdot(\rho u) = 0 \tag{8}$$

$$\frac{\partial}{\partial t}(\rho u) + \nabla\cdot(\rho u\otimes u) + \nabla p = -\rho\nabla\phi \tag{9}$$

$$\frac{\partial}{\partial t}(\rho {\rm e}) + \nabla\cdot\left[\rho u\left({\rm e} + p/\rho\right)\right] = -\rho u\cdot\nabla\phi \tag{10}$$

where ρ is the mass density, u is the fluid velocity, e is the specific total energy, and p is the thermal pressure, with

$$p = (\gamma-1)\rho\left({\rm e} - \frac{1}{2}u^2\right). \tag{11}$$

Note that the energy equation (Eq. (10)) is conservative for the total fluid energy, if one ignores the source terms due to gravity. This property is one of the main advantages of solving the Euler equations in conservative form: no energy sink due to numerical errors can alter the flow dynamics. Gravity is included in the system of equation as a *non stiff source term*. In this case, the system is not explicitly conservative and the total energy (potential + kinetic) is conserved at the percent level (see Sect. 4.3).

Let U_i^n denote a numerical approximation to the cell-averaged value of $(\rho, \rho\boldsymbol{u}, \rho{\rm e})$ at time t^n and for cell i. The numerical discretization of the Euler equations with gravitational source terms writes:

$$\frac{U_i^{n+1} - U_i^n}{\Delta t} + \frac{F_{i+1/2}^{n+1/2} - F_{i-1/2}^{n+1/2}}{\Delta x} = S_i^{n+1/2}. \tag{12}$$

The time centered fluxes $F_{i+1/2}^{n+1/2}$ across cell interfaces are computed using a second-order Godunov method (also known as Pieceweise Linear Method), with or without directional splitting (according to the user's choice), while gravitational source terms are included using a time centered, fractional step approach:

$$S_i^{n+1/2} = \left(0, \frac{\rho_i^n\nabla\phi_i^n + \rho_i^{n+1}\nabla\phi_i^{n+1}}{2}, \frac{(\rho u)_i^n\nabla\phi_i^n + (\rho u)_i^{n+1}\nabla\phi_i^{n+1}}{2}\right). \tag{13}$$

A general description of Godunov and fractional step methods can be found in Toro (1997). The present implementation is based on the work of Collela (1990) and Saltzman (1994). For sake of brevity, only its basic features are recalled here.

2.3.1. Single grid Godunov solver

In this section, I describe the basic hydrodynamical scheme used in RAMSES to solve Eqs. (8–10) at a given level. It is assumed that proper boundary conditions have been provided: the hydrodynamical scheme requires 2 ghost zones in each side and in each direction, even in the diagonal directions. Since in RAMSES the Euler equations are solved on octs of $2^{\rm dim}$ cells each, $3^{\rm dim}-1$ similar neighboring octs are required to define proper boundary conditions. The basic stencil of the PLM scheme therefore contains $6^{\rm dim}$ cells. This is not the case for PPM (Collela & Woodward 1984) for which 4 ghost zones are required in each side and in each direction. Since the AMR structure in RAMSES is based on octs ($2^{\rm dim}$ cells), PPM would be to expensive to implement in many aspects. One solution would be to modify the basic tree element and increase the number of cells per oct from $2^{\rm dim}$ cells to $4^{\rm dim}$ cells.

The resulting AMR structure would however loose part of its flexibility to adapt itself to complex flow geometry. The FLASH code (Fryxell et al. 2000) is an example of such an implementation, using the PPM scheme in a similar recursive tree structure, with however 8^{dim} cells per basic tree element.

For a given time step, we need to compute second-order, time-centered fluxes at cell interfaces. This is done in RAMSES using a Riemann solver, with left and right states obtained by a characteristics tracing step. A standard characteristic analysis is done first, by Taylor expanding the wave equations to second order and projecting out the waves that cannot reach the interface within the time step. These states are then adjusted to account for the gravitational field. If the chosen scheme is not directionally split, transverse derivative terms are finally added to account for transverse fluxes (Saltzman 1994). The slopes that enter into the Taylor expansion are computed using the Min-Mod limiter to ensure the monotonicity of the solution.

The Riemann solver used to compute the Godunov states is "almost exact", in the sense that a correct pressure at the contact discontinuity is obtained iteratively (typically, for strong shocks 10 Newton-Raphson iterations are required for single-precision accuracy of 10^{-7}). The only approximation relies in the assumption that the rarefaction wave has a linear profile. In the final step, fluxes of the conserved variables are computed using these Godunov states. The outputs of the single grid algorithm are therefore fluxes across cell interfaces.

Practically, this single grid module is applied to a large vector of stencils of 6^{dim} cells each. For a large Cartesian grid of N^{dim} cells, the CPU time overhead associated to this solution is rather large. Since the main time consuming part is the Riemann solver, the estimated CPU time overhead was found to be roughly 50%, 100% and 200% for dim = 1, 2 and 3 respectively. Since in any useful AMR calculation, the mesh structure is not a regular Cartesian grid, the actual overhead is much lower, although difficult to estimate in practice. Moreover, this solution is much easier to implement than any potentially faster alternative one can think of, and easy to optimize on vector and parallel supercomputers.

2.3.2. AMR implementation

This section describes how the solution is advanced in time within the present AMR methodology. Note that this procedure is recursive with respect to level ℓ (step 3).

1. Generate new refinements at level $\ell+1$ by conservative interpolation of level ℓ variables;
2. Compute the new time step Δt_ℓ using the CFL Courant condition and the constraint $\Delta t_\ell \le \Delta t_{\ell-1}$;
3. Advance the solution in time for level $\ell+1$, once in the single time step case, or twice for the adaptive time step case;
4. Modify the time step Δt_ℓ according to the synchronisation constraint $\Delta t_\ell = \Delta t_{\ell+1}$ for the single time step case or $\Delta t_\ell = \Delta t^1_{\ell+1} + \Delta t^2_{\ell+1}$ for the adaptive time step case;
5. Compute boundary conditions in a temporary buffer by conservative interpolation of level $\ell-1$ variables;
6. Compute fluxes using the single grid Godunov solver;
7. Replace the fluxes at coarse-fine interface by averaging the fluxes computed at level $\ell+1$;
8. For leaf cells, update variables using these fluxes;
9. For split cells, update variables by averaging down the updated variables of level $\ell+1$;
10. Build the new refinement map.

In RAMSES, boundary conditions are supplied to fine levels by a conservative linear reconstruction of coarse cell values (step 5). The actual interpolation scheme is a 3D generalization of the Min-Mod limiter (De Zeeuw 1993). The coarse solution is assumed to remain constant in time during the advance of the fine solution. For fine cells at coarse-fine boundaries and for the adaptive time step case only, the accuracy reduces thus from second to first order in time, but the global solution remains second order (Khokhlov 1998).

2.4. Time step control

The time step is determined for each level independently, using standard stability constraints for both N-body and hydrodynamical solvers.

The first constraint comes from the gravitational evolution of the coupled N-body and hydrodynamical system, imposing that Δt^ℓ should be smaller than a fraction $C_1 < 1$ of the minimum free-fall time

$$\Delta t_1^\ell = C_1 \times \min_\ell (t_{\mathrm{ff}}). \tag{14}$$

An additional constraint comes from particle dynamics within the AMR grid, imposing that particles move by only a fraction $C_2 < 1$ of the local cell size.

$$\Delta t_2^\ell = C_2 \times \Delta x^\ell / \max_\ell (v_{\mathrm{p}}). \tag{15}$$

A third constraint is imposed on the time step by specifying that the expansion factor a_{exp} should not vary more than $C_3 \simeq 10\%$ over one time step. This constraint is active only at early times, during the linear regime of gravitational clustering.

$$\Delta t_3^\ell = C_3 \times a_{\mathrm{exp}} / \dot{a}_{\mathrm{exp}}. \tag{16}$$

The last constraint is imposed by the Courant Friedrich Levy stability condition, which states that the time step should be smaller than

$$\Delta t_4^\ell = cfl \times \Delta x^\ell / \max_\ell (|u_x| + c, |u_y| + c, |u_z| + c) \tag{17}$$

where $cfl < 1$ is the Courant factor. In the coupled N-body and hydrodynamics case, the actual time step is equal to $\min(\Delta t_1^\ell, \Delta t_2^\ell, \Delta t_3^\ell, \Delta t_4^\ell)$.

2.5. Refinement strategy

The refinement strategy is the key issue for any AMR calculation. Bearing in mind that the overhead associated to the AMR scheme can be as large as a factor of 2 to 3 (see Sect. 2.3) compared to the corresponding uniform grid algorithm, the maximum fraction of the grid that can be refined lies in between 30% to 50%. One should therefore design a refinement strategy that allows for an accurate treatment of the underlying physical problem, but minimizes also the fraction of the volume to be refined.

For the N-body solver, the refinement strategy is based on the so-called "quasi-Lagrangian" approach. As in Kravtsov et al. (1997), the idea is to obtain a constant number of particles per cell. In this way, two-body relaxation effects can be minimized, as well as the Poisson noise due to particle discreteness effects. The latter effect can be damaging when coupling the N-body code to the hydrodynamics solver. The "quasi-Lagrangian" approach is implemented by refining cells at level ℓ if the dark matter density exceeds a level dependent density threshold, defined as

$$\rho_\ell = M_{\rm c} \times (\Delta x^\ell)^{-{\rm dim}} \tag{18}$$

where $M_{\rm c}$ is the maximum mass (or number of particles) per cell. For pure N-body simulations, $M_{\rm c}$ is usually chosen around 5–10 particles (Kravtsov et al. 1997), which gives a few particles per cell on average. For gas dynamics simulations, $M_{\rm c}$ should be chosen around 40-80 particles, in order to lower enough the Poisson noise. In this case, we obtain indeed more than 10 particles per cell on average. Note also that since for gas dynamics simulations, the total memory is dominated by the storage associated to the fluid variables, the number of particles par cell can be chosen much higher than for pure dark matter simulations.

As for the N-body solver, a "quasi-Lagrangian" approach can be implemented for the gas component, using level dependent density thresholds defined by

$$\rho_\ell = M_{\rm b} \times (\Delta x^\ell)^{-{\rm dim}}. \tag{19}$$

In order to follow the same Lagrangian evolution than the dark matter component, the typical baryonic mass per cell $M_{\rm b}$ can be derived as

$$M_{\rm b} = M_{\rm c} \frac{\Omega_{\rm b}}{\Omega_{\rm m} - \Omega_{\rm b}}\cdot \tag{20}$$

For pure gas dynamics applications, other refinement criteria can be used (see Khokhlov 1998, for more examples). In RAMSES, only refinement criteria based on gradients of the flow variables have been implemented: for each cell i and for any relevant flow variable q (pressure, density, Mach number...), its gradient is computed using the $2 \times$ dim neighboring cells. If this gradient, times the local mesh spacing, exceeds a fraction of the central cell variable

$$\nabla q_i \geq (\nabla q)^\ell_{\max} = C_q \frac{q_i}{\Delta x^\ell} \tag{21}$$

then cell i is refined. The parameter C_q is a free parameter that need to be specified by the user. A similar criterion based on second derivatives of the flow variables has also been implemented.

The last refinement criterion implemented in RAMSES is purely spatial: for each level, refinements are not allowed outside a sphere centered on the box center. This last criterion allows the user to refine the computational mesh only in the center of the box, in order to follow properly the formation of a single structure, without spending to much resources in refining also the surrounding large scale field. The radius of this spherical region, noted R_ℓ, can be specified for each level independently.

2.6. Cosmological settings

RAMSES can be used for standard fluid dynamics or N-body problems, with periodic, reflecting, inflow or outflow boundary conditions. For the present paper, RAMSES is however used in the cosmological context. The N-body solver and the hydrodynamics solver are both implemented using "conformal time" as the time variable. This allows a straightforward implementation of comoving coordinates, with minor changes to the original equations. The details of these so-called "super-comoving coordinates" can be found in Martel & Shapiro (1998) and references therein. The idea is to perform the following change of variables

$${\rm d}\tilde{t} = H_0 \frac{{\rm d}t}{a^2} \quad \text{and} \quad \tilde{x} = \frac{1}{a}\frac{x}{L} \tag{22}$$

$$\tilde{\rho} = a^3 \frac{\rho}{\Omega_{\rm m}\rho_{\rm c}} \quad \text{and} \quad \tilde{P} = a^5 \frac{P}{\Omega_{\rm m}\rho_{\rm c} H_0^2 L^2} \tag{23}$$

$$\tilde{\boldsymbol{u}} = a \frac{\boldsymbol{u}}{H_0 L} \tag{24}$$

where H_0 is the Hubble constant, $\Omega_{\rm m}$ is the matter density parameter, L is the box size and $\rho_{\rm c}$ is the critical density. In the specific case $\gamma = 5/3$, Eqs. (1) and (8–10) remain unchanged, at the exception of the Poisson equation which now reads

$$\triangle_x \tilde{\phi} = \frac{3}{2} a \Omega_{\rm m} (\tilde{\rho} - 1). \tag{25}$$

If $\gamma \neq 5/3$, a single additional source term must be included in the right-hand side of the energy conservation equation (Eq. (10)). These "super-comoving coordinates" simplify greatly the introduction of comoving variables in the equations.

3. Tests of the code

In this section, I present tests of increasing complexity for both the N-body solver and the hydrodynamical solver. These tests are also useful to choose the correct parameters for realistic cosmological applications described in the last section.

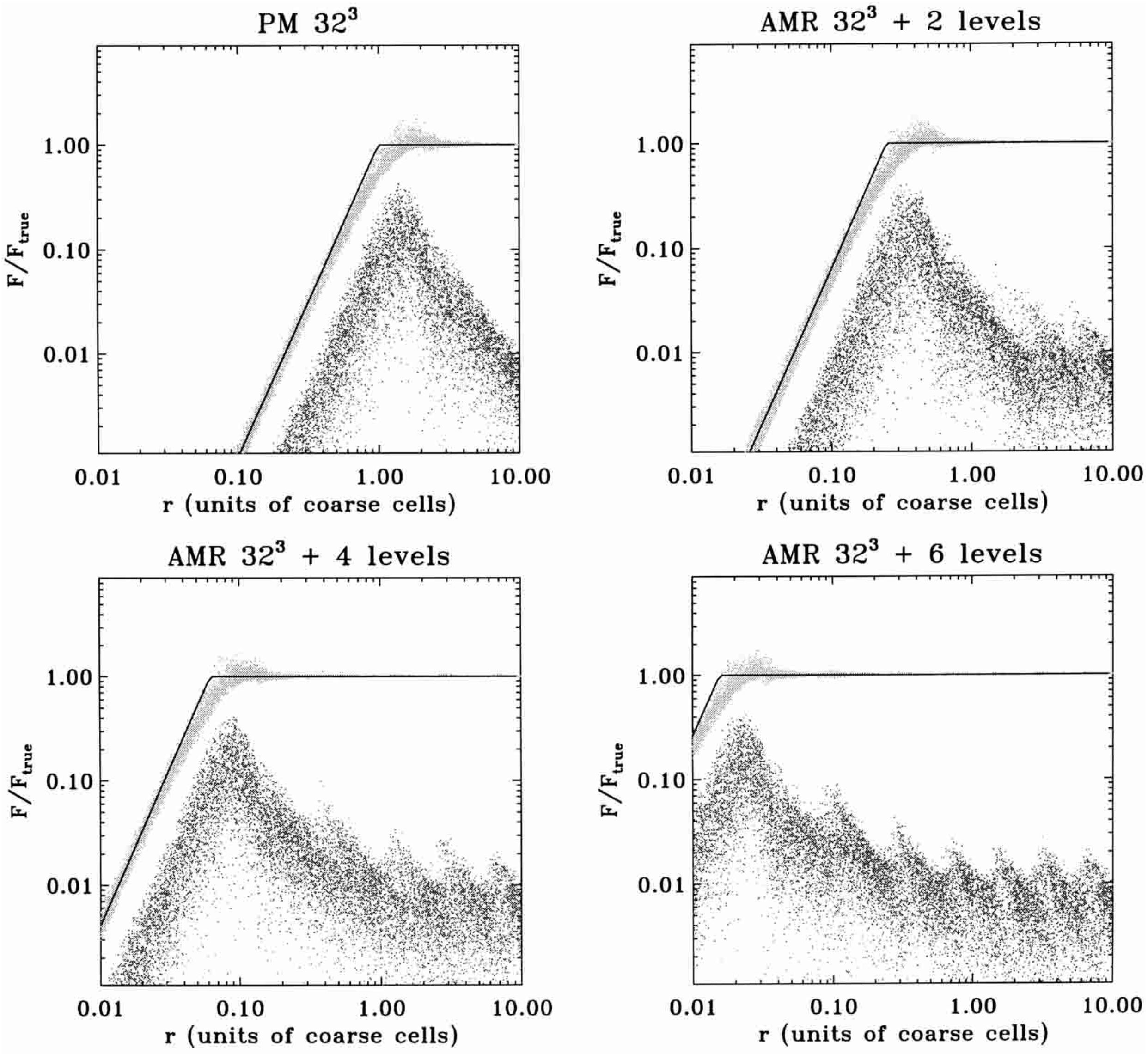

Fig. 1. Acceleration of massless test particles dropped randomly around single massive particles, whose positions are also chosen randomly in the box. The coarse grid has 32^3 cells. The number of refinement levels is progressively increased from 0 to 6, with increased spatial resolution around the massive particles. The radial AMR acceleration divided by the true acceleration is shown as light grey dots (versus radius in units of coarse cell size). The same ratio for the tangential AMR acceleration is shown as dark grey dots. The force corresponding to an homogeneous sphere with radius equal to the smallest cell length is also plotted for comparison (solid line).

3.1. Acceleration around a Point Mass

Particles of unit mass are placed randomly in the computational box, whose coarse grid is defined by $n_x = n_y = n_z = 32$. Test particles are then dropped randomly in order to sample the acceleration around each massive particle. The AMR grid is built around each central particle. For that purpose, refinement density thresholds were set to $\rho_\ell = 0$ for each level. An increasing number of refinement levels was used, from $\ell_{\max} = 0$ to $\ell_{\max} = 6$, the latter case corresponding to a formal resolution of 2048^3. Mesh smoothing was performed with $n_{\rm expand} = 1$.

Figure 1 shows the resulting radial and tangential accelerations, divided by the true $1/r^2$ force. The tangential acceleration gives here an indication of the level of force anisotropy and accuracy. Note that the acceleration due to the ghost images of the massive particle (periodic boundary conditions) was substracted from the computed acceleration (using the Ewald summation method). For comparison, the acceleration of an homogeneous sphere (with radius equal to the cell size of the maximum refinement level) is also plotted in Fig. 1 as a solid line: the AMR acceleration appears to provide a slightly lower spatial resolution (rouhly 1.5 cell size). At lower radius, the force smoothly goes to zero, exactly as for a PM code of equivalent dynamical range. At lower radius, the force anisotropy is also the same as for a PM code of equivalent dynamical range. On the other hand, at higher radius, the force anisotropy remains close to 1%. Contrary to a single grid PM solver, the force error does not decrease monotonically as radius increases. Here, the error level remains roughly constant (at the percent level), since the spatial resolution also decreases as radius increases. In fact, the AMR force on a given particle corresponds to a single grid PM force whose cell size is equal to that of the particle's current level. As one goes from one level to the next, discontinuities in the force remain also at the percent level.

3.2. Acceleration of particles in a ΛCDM simulation

In order to assess the quality of the gravitational acceleration computed by RAMSES in a cosmological situation, we consider now a set of 64^3 particles obtained in a ΛCDM simulation, at redshift $z = 0$. In this way, we are able to quantify the force errors in a typical hierarchical clustering configuration, with the corresponding mesh refinements structure. The coarse grid was defined by $n_x = n_y = n_z = 32$ and each particle was assigned a mass $m_{\rm p} = 1/8$. The adaptive mesh was built using refinement density thresholds $\rho_\ell = 5 \times 8^\ell$ for each level ℓ. Each cell is therefore refined if it contains more than 40 particles, with a roughly constant number of particles per cell after each refinement (between 5 and 40). Mesh structures associated to this particle distribution are shown in the last section of the paper (Fig. 10).

For each level of refinement, the AMR force is then compared to the PM force of equivalent spatial resolution (see Fig. 2). For particles sitting at the coarse level ($\ell = 0$), the force is by construction exactly equal to the PM force with 32^3 cells (results not shown in the figure). For levels $\ell = 1$, $\ell = 2$, $\ell = 3$ and $\ell = 4$, the AMR force is compared to the PM force with respectively 64^3, 128^3, 256^3 and 512^3 cells. In Fig. 2, each panel shows the difference between the AMR force and the PM force for each level. The number of particles sitting at each level is indicated in the upper-left part of each panel. The mean force error and the standard deviation is indicated in the lower-left part of each panel. Although the error distribution is strongly non Gaussian, its typical magnitude remains at the percent level in all cases. Note that errors are larger for forces of intermediate and small values, indicating that those particles might be sensitive to the boundary conditions (tidal field) imposed on the level boundaries (this is the main source of inaccuracy in the N-body scheme). On the other hand, for particles with strong acceleration, the AMR force is almost indistinguishable from the PM force of equivalent resolution.

3.3. Shock tube

The initial conditions are defined by a left state given by $\rho_{\rm L} = 1$, $u_{\rm L} = 0$ and $P_{\rm L} = 1$ and by a right state given by $\rho_{\rm R} = 0.125$, $u_{\rm R} = 0$ and $P_{\rm R} = 0.1$ for a $\gamma = 1.4$ fluid. This test (also called Sod's test) is interesting because it captures all essential features of one dimensional hydrodynamical flows, namely a shock wave, a contact discontinuity and a rarefaction wave. While the latter wave remains continuous, the 2 former features are discontinuous. Modern shocks capturing methods like the one used in RAMSES spread shock fronts over 2 to 3 zones. Contact discontinuities are usually more difficult to capture (say 6 to 10 cells), and the spreading usually increases with the number of time step. This numerical smoothing is responsible for the dissipation of the scheme. AMR technique allows one to increase the spatial resolution around the discontinuities and therefore to minimize the numerical dissipation. In the present application, the refinement criteria are based on pressure, density and Mach number gradients (see Sect. 2.5), with parameter $C_\rho = C_{\rm P} = C_{\rm M} = 0.01$. The maximum number of refinements was set to $\ell_{\max} = 6$, for a coarse level mesh size $n_x = 64$. Mesh smoothing (see Sect. 2.1.1) is performed using $n_{\rm expand} = 1$. Note that the refined mesh is built before the beginning of the simulation. The time step is controlled by a Courant number $cfl = 0.8$. Results are shown at time $t = 0.245$ and compared to the analytical solution in Fig. 3. The shock front and the contact surface are refined up to the maximum refinement level: the formal resolution is therefore 4096. The total number of cells (counting both split and leaf cells) is only 560, or 14% of the corresponding uniform mesh size. 69 time steps were necessary at the coarse level, while 4416 time steps were necessary at level $\ell = 6$. It is worth mentioning that pressure and velocity remain remarkably uniform across the contact discontinuity, and no side effects due to the presence of discrete refinement ratio are noticeable.

3.4. Planar Sedov blast wave

The last test, though interesting and complete, is not a very stringent one, since it involves a rather weak shock. In order to test the ability of RAMSES to handle strong shocks (a common feature in cosmology), let us consider the planar Sedov problem: the computational domain is filled with a $\gamma = 1.4$ fluid with $\rho_0 = 1$, $u_0 = 0$ and $P_0 = 10^{-5}$. A total (internal) energy $E_0 = 1/2$ is deposited in the first cell only at $x = 0^+$. Note that here again the refined mesh is built before the beginning of the simulation. Reflexive boundary conditions are considered. The grid is defined by $n_x = 32$ with 6 levels of refinement. The only refinement criterion used here is based on pressure gradients, with $C_{\rm P} = 0.1$. Mesh smoothing is guaranteed by $n_{\rm expand} = 1$. The Courant number is set to $cfl = 0.8$. Very rapidly, a self-similar flow builds up, following the analytical solution described in Sedov (1993). Simulation results are shown for different output times and compared to the analytical solutions. Note that the shock front propagates exactly at the correct speed. The numerical solution closely matches the analytical one, without any visible post-shock oscillations. 239 time steps only were necessary at the coarse level, but 15296 time steps were necessary at the finest refinement level. The total number of cells

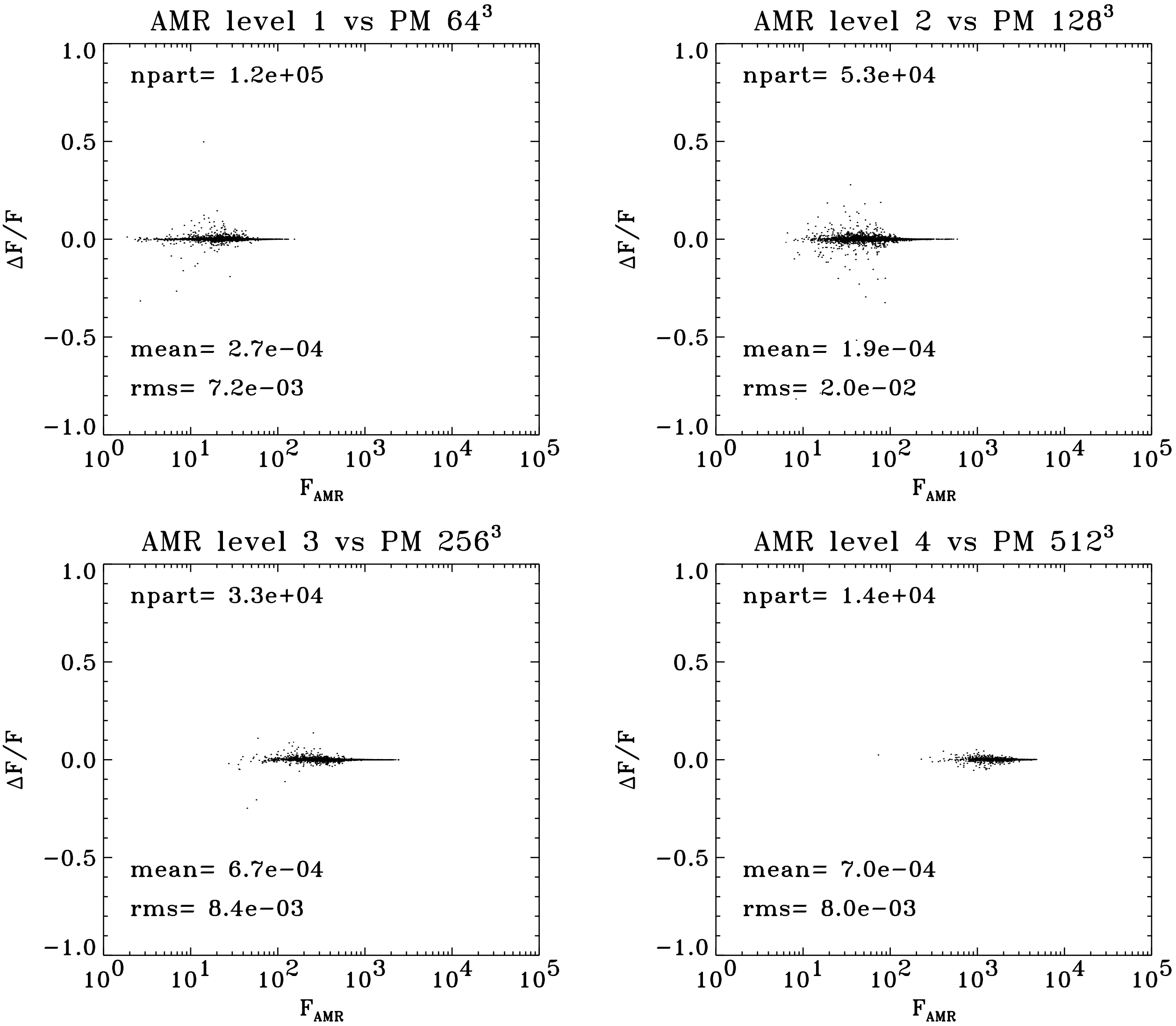

Fig. 2. Particle positions obtained in a ΛCDM simulation are considered in this test. Each panel shows the force error for particles sitting at different levels of refinement. The error is defined as the difference between the AMR force and the force computed by a PM code of equivalent spatial resolution. In each panel, the average and the variance of the error are also shown.

(including split cells) in the adaptive mesh structure is only 130, to be compared with 2048 cells for the uniform grid of equivalent spatial resolution (4.3%). Due to the refinement criterion used here, the adaptive mesh mainly concentrates the computational effort around the shock front. In one dimension, as it is the case here, discontinuities like shocks are quite inexpensive to deal with: if one adds one level of refinement, the total number of cells increases by a constant (and small) amount. For two- and three-dimensional calculations, the situation is much more demanding: since shocks and contacts discontinuities are surface waves, increasing the resolution by a factor of 2 corresponds to increasing the total number of cells by a factor of 2 for dim = 2 and 4 for dim = 3. Therefore, we have to face the possibility of stopping at some level the refinement hierarchy and investigate what happens to the numerical solution in this case.

3.5. Strong shock passing through a Coarse–Fine interface

It is well known that in any AMR calculations, discontinuities in the flow (like the one discussed in the previous sections) must be refined up to the maximum level, in order to obtain accurate results (Berger & Collela 1989; Khokhlov 1998). Unfortunately, it is not always possible to satisfy this rule because of memory limitations, even on modern computers. One has therefore to consider cases for which discontinuities leave or enter regions of different spatial resolution. The situation is especially sensitive for contact surfaces, since as soon as the code spreads them over, say, 6 cells, no matter how much one refines them afterwards, they will preserve their original thickness. Shock waves, however, have a self-steepening mechanism that allows them to adapt to the local resolution and restore their

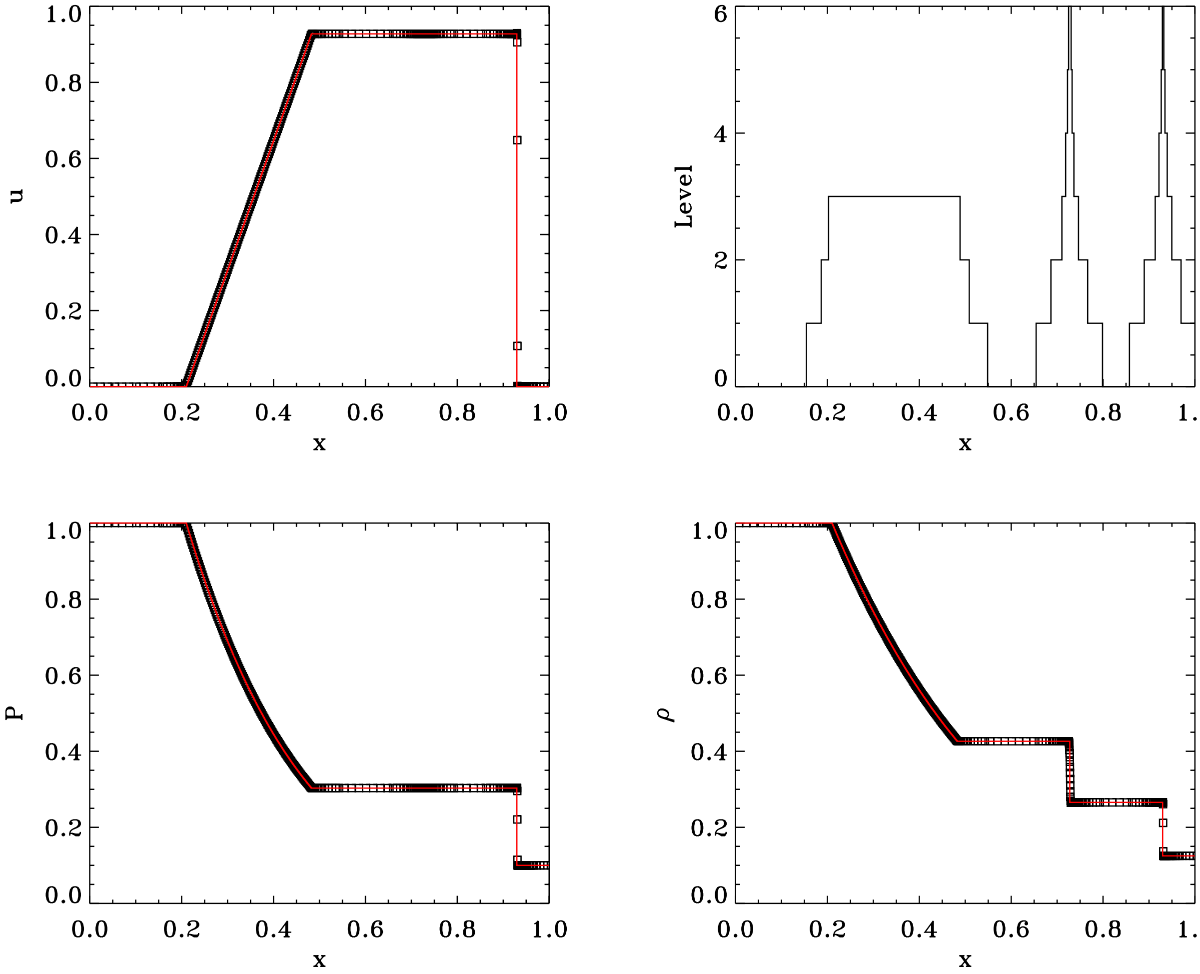

Fig. 3. Shock Tube Test: density, velocity, pressure and refinement level as a function of position at time $t = 0.245$. Numerical results are shown as squares, and compared to the analytical solutions (solid lines). See text for details.

sharp profile over 2 to 3 cells only. The price to pay for this interesting property is the appearance of post-shock oscillations after the front has entered a high-resolution region. To illustrate this, Khokhlov (1998) proposed a simple test based on the propagation of a strong shock wave across a coarse–fine interface. Khokhlov's test is reproduced here using the following parameters: the shock Mach number is set to $M = 5000$ with $\gamma = 5/3$. The base grid resolution is set to $n_x = 256$ and the Courant number is set to $cfl = 0.5$.

The following three cases have been considered:

1. the whole computational domain is refined up to $\ell = 1$;
2. the computational domain is refined up to $\ell = 1$ only left to $x = 234$;
3. the computational domain is refined up to $\ell = 2$ right to $x = 234$ and up to $\ell = 1$ otherwise.

The resulting density profiles are shown in Fig. 5. While in the 2 former cases, the density profiles show no visible oscillations, the latter case does show small oscillations of the order of 5%. This is a direct consequence of the abrupt change of spatial resolution between the 2 levels of refinement (see the discussion in Berger & Collela 1989). To summarize, if shock waves move from high- to low-resolution regions, spurious effects associated to the mesh structure are undetectable. This is not the case in the opposite situation, which causes spurious (though small) post-shock oscillations. Note however that for weak shocks the effect is undetectable (Berger & Collela 1989). In cosmology, it is worth mentioning that, since the basic features are accretion shocks, we are always in a favorable situation: strong shocks originate in high-density (high-resolution) regions, and propagates outwards, in a low-density (low-resolution) background. To my opinion, this fundamental property allows us to use safely adaptive mesh technique in cosmological simulations.

3.6. Spherical Sedov blast wave

We now consider a very difficult test for Cartesian grids like the one used in RAMSES: the spherical Sedov test. In contrary to the planar, 1D case, the spherical blast wave is now fully three-dimensional and pretty far from

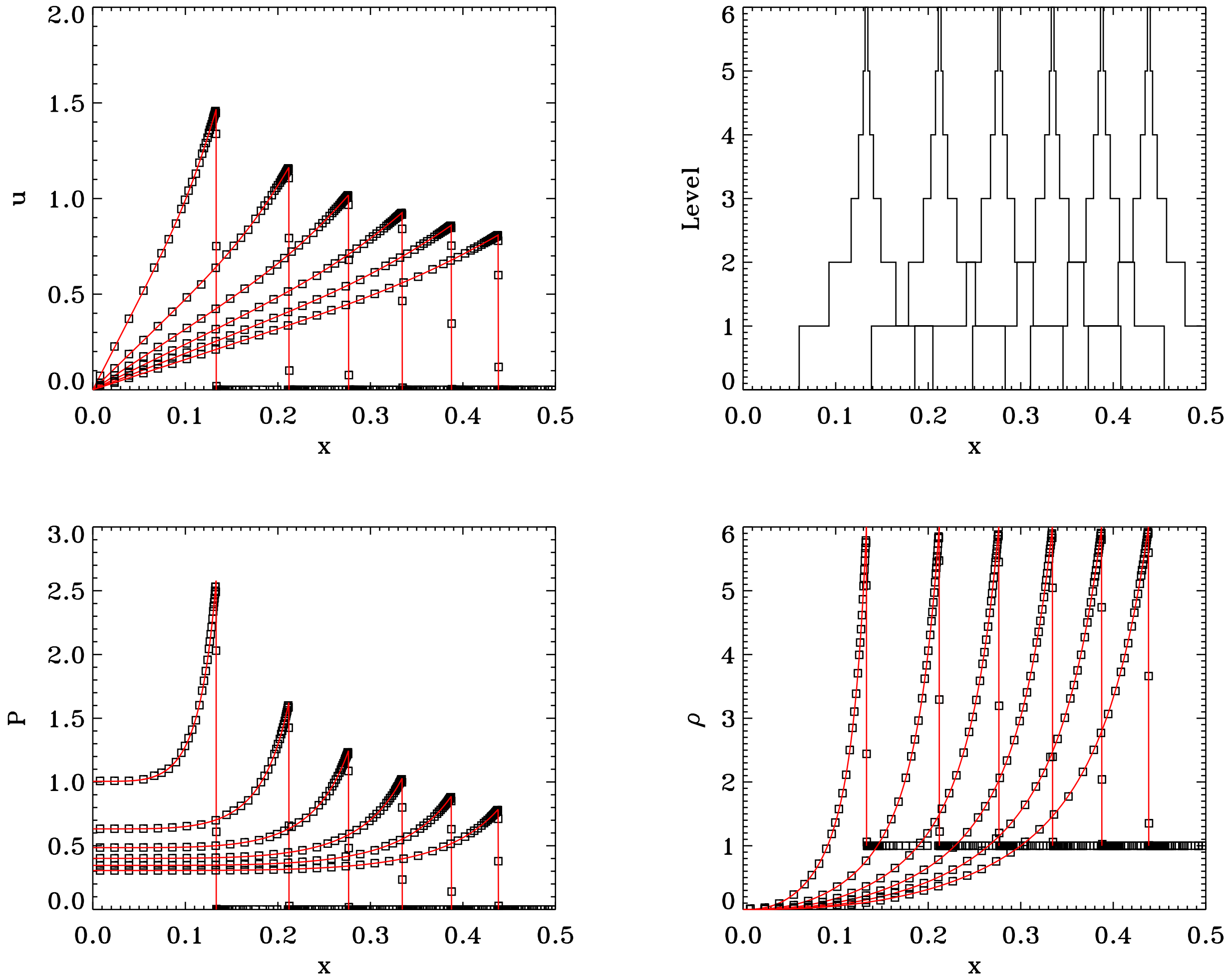

Fig. 4. Planar Sedov Blast Wave Test: density, velocity, pressure and refinement level as a function of position for times $t = 0.05$, 0.1, 0.15, 0.2, 0.25 and 0.3. Numerical results are shown as squares, and compared to the analytical solutions (solid lines). See text for details.

the natural geometry of the code. Moreover, as stated before, shock waves in 3D are essentially two-dimensional: the total number of cells necessary to cover the shock front scales with spatial resolution as

$$N_{\rm cells} \propto \left(\frac{R_{\rm s}}{\Delta x}\right)^{\rm dim-1} \tag{26}$$

where $R_{\rm s}$ is the curvature radius of the shock. For dim $= 3$, one clearly sees that the number of required cells quickly explodes. On the other hand, for the Sedov blast wave test, it is more interesting to keep the *relative* thickness of the shock low enough to capture the true solution. As we have seen in the last section, if one degrades the resolution as the shock propagates outwards, no spurious effects are expected. In RAMSES, we can enforce a position–dependent spatial resolution by forbidding a given level of refinement to be activated if the radius of the cell is larger than a given threshold (see Sect. 2.5). The run parameters are therefore the followings: the coarse grid size is set to $n_x = n_y = n_z = 32$ and the maximum level of refinement is chosen to be $\ell_{\rm max} = 6$. The maximum refinement radius for each level is given by

$$R_\ell = 2^{5-\ell} \quad \text{for} \quad 0 \le \ell \le 5. \tag{27}$$

We use refinement criteria based on pressure gradients with $C_P = 0.5$ and mesh smoothing parameter $n_{\rm expand} = 1$. The fluid is supposed initially at rest with $\rho_0 = 1$ and $P_0 = 10^{-5}$. A total (internal) energy $E_0 = 1$ is deposited in the 8 central cells only. The refined mesh is here again built before the beginning of the time integration. We assume $cfl = 0.8$ and $\gamma = 1.4$. We use here a single time step for all levels, since in this particular case, this is the fastest solution.

Results are shown in Fig. 6 and compared to the analytical solutions of Sedov (1993) for 3 different output times. Each quantity represents a volume-average value over spherical bins, whose thicknesses correspond to the local resolution. Each quantity was also rescaled according to the (time-dependent) analytical post-shock values (labeled with an "s") for sake of visibility. Error bars are computed using the standard deviation of the numerical

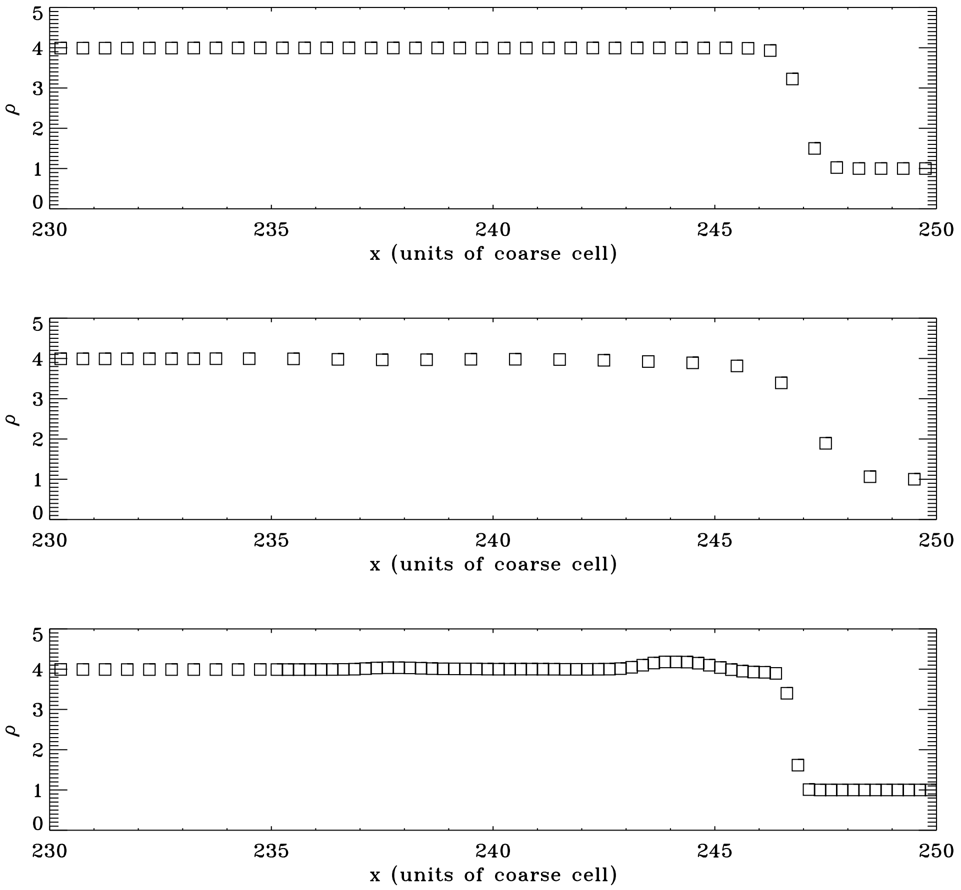

Fig. 5. Strong shock passing through a Coarse–Fine interface with Mach number $M = 5000$ and $\gamma = 5/3$, computed with $cfl = 0.5$. The upper plot shows the reference case with a 256 cells coarse grid, uniformly refined up to level $\ell = 1$ (without any coarse–fine boundary). The middle figure shows the case where the shock goes through a fine–to–coarse boundary (located around $x \simeq 234$), while the bottom figure shows the case where the shock goes to a coarse–to–fine boundary (located around the same place). In the latter case, perturbations of the order of 5% are generated in the post–shock flow.

solution from the mean value in each spherical bin. The agreement with the analytical solution is remarkable, considering that the mesh has a Cartesian geometry. The main departure is found in the velocity profile at a radius around 60% of the shock radius. Similar results were obtained by Fryxell et al. (2000). An easy way of solving this problem would be to lower the pressure gradients threshold C_{P}, which would directly increase the resolution in this region, at the expense of increasing the total number of cells. Oscillations due to spurious mesh reflections are not visible in the radial profiles. Direct inspection of the 3D data shows that the only systematic effect is the departure from spherical symmetry due to the Cartesian nature of the mesh. In Fig. 6, the volume-averaged refinement level is shown as a function of radius for different times. Due to the maximum refinement radii we used (Eq. (27)), the adaptive mesh evolution is also self-similar, though in a piecewise constant manner. The total number of cells (and therefore the memory used) remains roughly constant over the calculation (around 10^6 cells, including split cells). The interest of using a tree-based approach for building the adaptive mesh appears clearly in this test, since the mesh structure follows as closely as possible the spherical shape of the shock front.

3.7. Zel'dovich pancake

In this section, typical conditions encountered in cosmological simulations are addressed using the Zel'dovich pancake test. This test is widely used to benchmark cosmological hydrodynamics codes (Cen 1992; Ryu et al. 1993; Bryan & Norman 1997; Teyssier et al. 1998), since it encompasses all the relevant physics (gravity, hydrodynamics and expansion). It can be thought as a single mode analysis of the collapse of random density perturbations, a first step towards the study of the fully three-dimensional case. The initial conditions are defined for a given starting redshift z_{i} in an Einstein-de Sitter universe ($\Omega_{\mathrm{m}} = 1$, $\Omega_{\mathrm{b}} = 0.1$), using a sinusoidal density perturbation of *unit wavelength*, i.e. of the form

$$\frac{\delta\rho}{\rho} = \frac{1 + z_{\mathrm{c}}}{1 + z_{\mathrm{i}}} \cos\left(2\pi x\right) \tag{28}$$

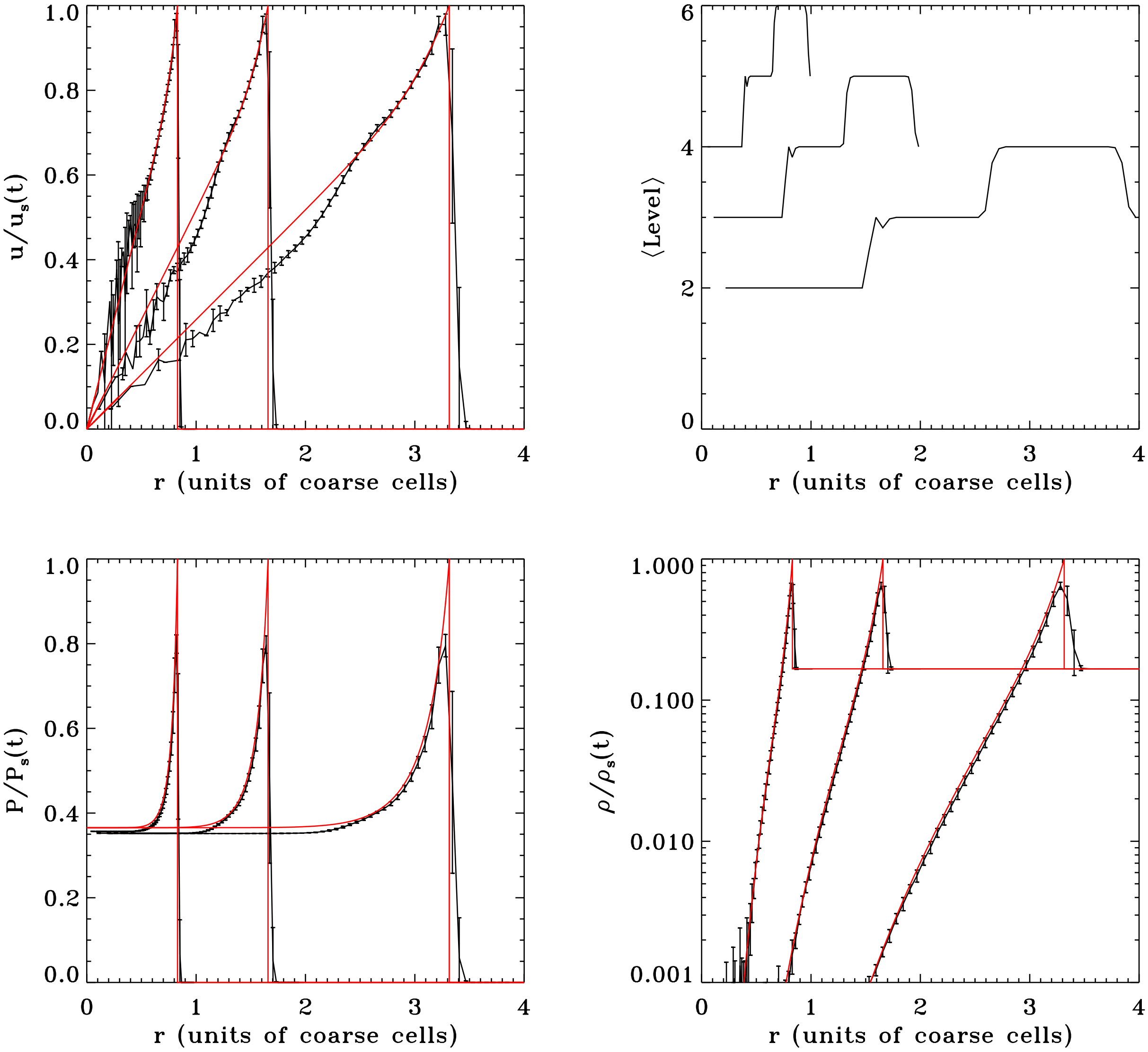

Fig. 6. Spherical Sedov blast wave test: rescaled density, velocity, pressure and volume-averaged refinement level as a function of radius for times $t = 10^{-4}$, 5.7×10^{-4} and 3.2×10^{-3}. Numerical results (solid lines with error bars) are compared to the analytical solutions (solid lines). See text for details.

where x is the comoving distance to the pancake mid-plane (from now on, we always use super-comoving coordinates, as defined in Sect. 2.6). The initial velocity field is set according to the linear theory of gravitational instability

$$u = -\frac{1}{2\pi}\frac{1+z_{\rm c}}{(1+z_{\rm i})^{3/2}}\sin\left(2\pi x\right). \tag{29}$$

The collapse redshift is chosen to be $1 + z_{\rm c} = 10$ and the initial redshift is $1 + z_{\rm i} = 100$. The initial baryons temperature was set to a very low arbitrary value, consistent with a negligible background temperature.

The coarse grid is defined by $n_x = 32$. We use $N_{\rm p} = 256$ particles for the dark matter component. The maximum level of refinement was set to $\ell_{\rm max} = 6$, corresponding to a formal resolution of 2048. Two different cases are investigated: in the first run, both pressure gradients and gas density thresholds (quasi-Lagrangian mesh) are used to build the adaptive mesh, with

$$\rho_\ell = 2\Omega_{\rm b}\rho_{\rm c}\frac{\Delta x_0}{\Delta x_\ell} \quad \text{and} \quad C_{\rm P} = 0.5 \tag{30}$$

while in the second case, only gas density thresholds are used to trigger new refinements.

Results are shown in Fig. 7 for both cases. For the first case, the two accretion shock fronts are refined up to the maximum refinement level, and are therefore very sharp. For the second case, however, the shock fronts are not refined at all. The shock waves are traveling outwards, from the high-resolution region in the pancake center, to the low-resolution background. In light of what have been discussed in the previous sections, this explains why no oscillations (due to potential spurious reflections at level boundaries) are visible. It is worth mentioning that both sets of profiles are almost indistinguishable in the center

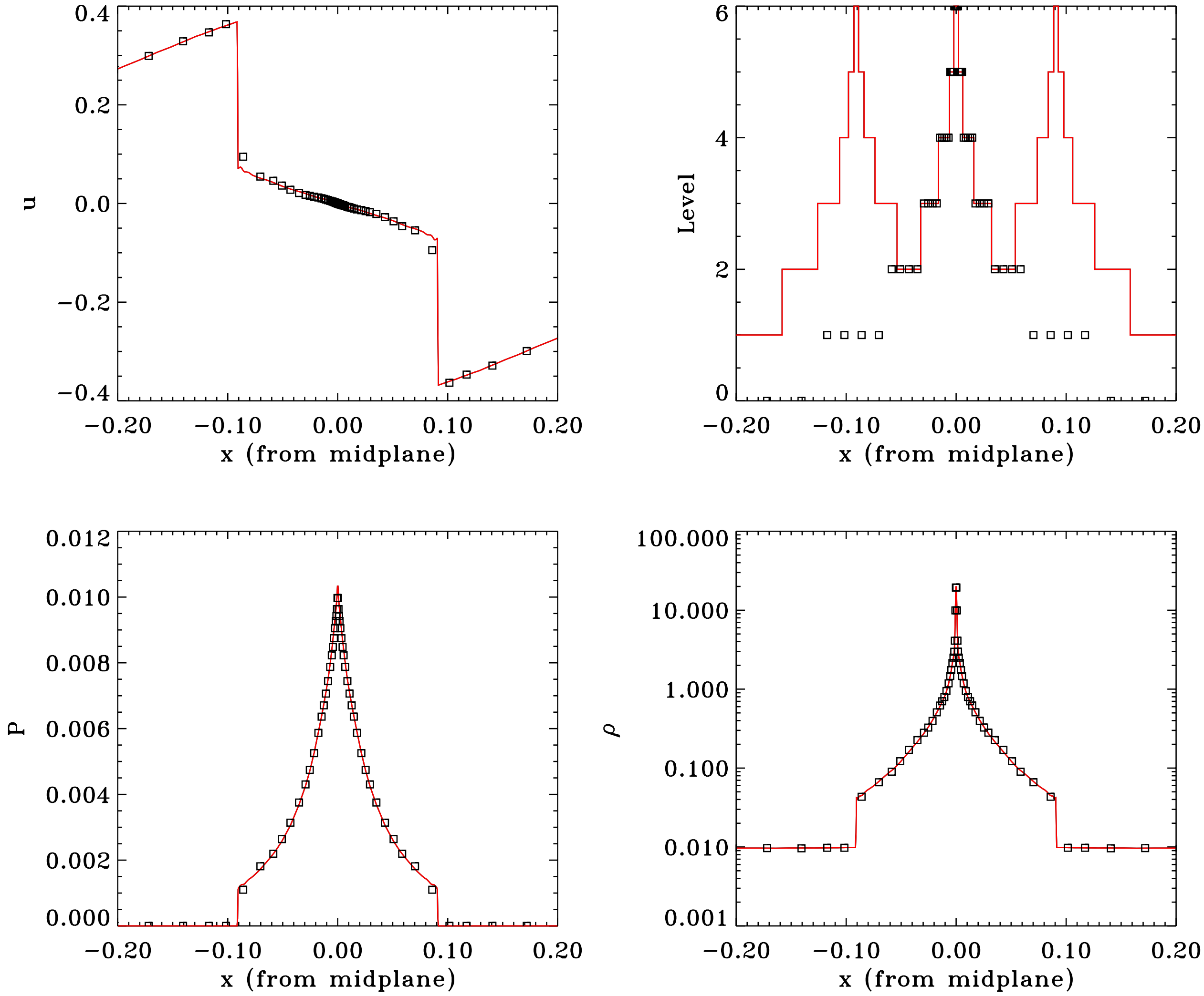

Fig. 7. Zel'dovich Pancake Test: density, velocity, pressure and refinement level as a function of position from the pancake mid-plane at $z = 0$. The solid line shows AMR results if refinements are activated using both density thresholds and pressure gradients. This explains why the 2 accretion shocks are refined. The squares show AMR results if refinements are activated using only density thresholds. See text for details.

of the pancake. This last test is very encouraging, since it allows us to avoid refining shock fronts in cosmological simulations. The opposite situation would have been dramatic, because of the large filling factor of cosmic shock waves (especially in 3D), which would result in a very large memory overhead, and because it would trigger collisionality in the dark matter particles distribution.

3.8. Spherical secondary infall

The last test, while interesting, is not very stringent, since it is very close to the natural, Cartesian geometry of the code. An analytical solution describing the fully non-linear collapse of spherical density perturbations was found by Bertschinger (1985), for both pure dark matter and pure baryons fluids. The initial conditions defining the system are the followings: a completely homogeneous Einstein-de Sitter universe (with $\Omega_{\rm m} = 1$) contains a single mass perturbation δM_0 at some initial epoch t_0. Surrounding this initial seed, shells of matter with increasing radius starts expanding within the Hubble flow, but finally decouples from the expansion at some "turn around" time, and the corresponding turn around *proper* radius, given by

$$r_{\rm ta}(t) = \left(\frac{4}{3\pi}\frac{t}{t_i}\right)^{8/9}\left(\frac{3}{4\pi}\frac{\delta M_0}{\rho_c}\right)^{1/3}. \qquad (31)$$

Since in the problem, no other time- or length-scale are involved, the overall evolution is self-similar.

In Kravtsov et al. (1997), the secondary infall test was successfully passed by the ART code for the pure dark matter case. Results obtained by RAMSES are very close to the ones obtained by the ART code, which is reassuring, since both codes have almost the same N–body solver. They are not presented here. Rather, we investigate the purely baryonic self–similar infall, so as to validate the hydrodynamics solver coupled to gravity and cosmological expansion.

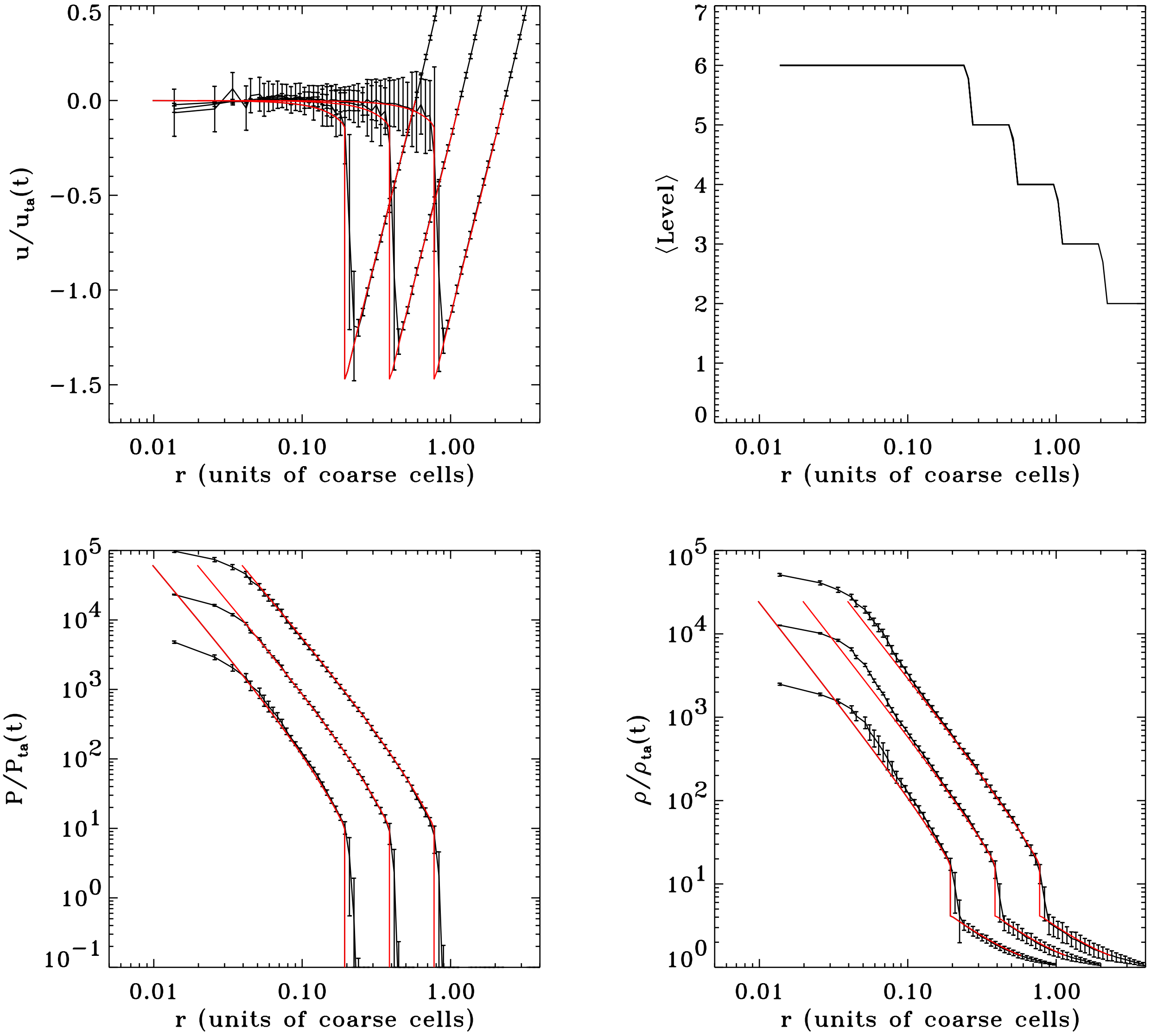

Fig. 8. Secondary Infall Test: rescaled density, velocity, pressure and volume-averaged refinement level as a function of radius (in units of coarse cells length) for expansion factors $a = 64a_i$, $512a_i$ and $4096a_i$. Numerical results (solid lines with error bars) are compared to the analytical solutions of Bertschinger (1985) (solid lines). See text for details.

The periodic box is initially filled with a critical density cold gas with $\gamma = 5/3$. A single dark matter particle with mass $m_\mathrm{p} = 1/8$ is placed as initial seed in the center of the computational domain. The coarse grid is defined by $n_x = n_y = n_z = 32$ and the maximum level of refinement was set to $\ell_\mathrm{max} = 6$, providing us a formal spatial resolution of 2048^3. Before the beginning of time integration, the mesh is refined around the central seed using a maximum refinement radius for each level given by

$$R_\ell = 2^{3-\ell} \quad \text{for} \quad 0 \le \ell \le 5 \tag{32}$$

in units of coarse cell size. The resulting mesh structure can be seen in Fig. 8 in a volume-averaged radial representation, with roughly 10^5 cells in the AMR tree, including split cells. No pressure gradients criterion is used, so that shock fronts are not refined. We use a Courant factor $cfl = 0.5$. Starting at expansion factor $a_i = 10^{-5}$, three output times were analyzed ($a \simeq 64a_i$, $512a_i$ and $4096a_i$). The final epoch was reached in 86 coarse time steps only, but 5504 time steps at the maximum level of refinement.

The resulting *rescaled* density, pressure and velocity profiles are plotted in Fig. 8 and compared to the analytical solution of Bertschinger (1985). Error bars are computed using the standard deviation of the numerical solution with respect to the average radial value. The scaling relations for velocity, density and pressure are obtained using their "turn around" values

$$\rho_\mathrm{ta}(t) = (6\pi G t^2)^{-1} \tag{33}$$

$$u_\mathrm{ta}(t) = \frac{r_\mathrm{ta}(t)}{t} \tag{34}$$

$$P_\mathrm{ta}(t) = \rho_\mathrm{ta}(t)\frac{r_\mathrm{ta}(t)^2}{t^2}\cdot \tag{35}$$

We find a very good agreement between numerical and analytical profiles, down to a radius of 2 fine cells, the actual resolution limit of the code. As the shock propagates outwards, no spurious reflection appears, as expected.

4. Application to cosmology: Structure formation in a ΛCDM universe

In this section, results obtained by RAMSES for a N-body and hydrodynamical simulation of structure formation in a ΛCDM universe are reported. The box size was set to $L = 100$ h^{-1} Mpc, as a good compromise between cosmic variance and resolution. The influence of the chosen box size on the results are not investigated in this paper. On the other hand, the convergence properties of the solution are examined by varying the mass and spatial resolution using 6 different runs, whose parameters are listed in Table 1 below. Numerical results are also compared to analytical results obtained in the framework of the halo model. This simple theory predicts various quantities for both gas and dark matter distributions, and has already proven to successfully reproduce results obtained in various numerical simulations (see Sect. 4.5). A careful comparison between the analytical and the numerical approach will serve us as a guide to investigate our understanding of structure formation in the universe.

4.1. Initial conditions

An initial Gaussian random field was generated for the highest resolution run on a 256^3 particle grid and (periodic) box length $L = 100$h^{-1} Mpc. The transfer function of Ma (1998) for a flat ΛCDM universe was used and normalized to the COBE data (White & Bunn 1995), with the following cosmological parameters

$$\Omega_{\rm m} = 0.3 \quad \Omega_\Lambda = 0.7 \quad \Omega_{\rm b} = 0.039 \tag{36}$$

$$h = 0.7 \quad \sigma_8 = 0.92. \tag{37}$$

The high resolution grid was then degraded twice (down to 128^3 and 64^3) to provide consistent initial conditions for our low resolution runs. In this way, a direct comparison between the 3 simulations is made possible. The corresponding mass resolution (corresponding to individual particle masses for a pure dark matter universe) is $M_0 = 5\times10^9\ M_\odot$ ($4\times10^{10}\ M_\odot$ and $3\times10^{11}\ M_\odot$). Particles were initially displaced according to the Zel'dovich approximation up to a starting redshift $1 + z_i = 72$ (51, 36) for the 256^3 (128^3, 64^3) grid. The initial gas density and velocity field was perturbed according to the linear theory of gravitational clustering, using the same density and displacement fields as for dark matter. The initial gas temperature was set to $T = 548(1 + z_i)^{-2}$ K, in order to recover the correct thermal history of baryons after recombination, when neglecting re-ionization. The adiabatic index was set to $\gamma = 5/3$, and a fully ionized, primordial H and He plasma was considered, with mean molecular weight $\mu = 0.59$.

Table 1. RAMSES parameters for our six ΛCDM simulations. In each case, the box size was set to $L = 100$ h^{-1} Mpc.

Name	$N_{\rm part}$	$\ell_{\rm max}$	$N_{\rm cell}$	$\Delta x_{\rm min}$	$N_{\rm step}$	
				h^{-1}kpc	$\ell = 0$	$\ell_{\rm max}$
P064L0	64^3	0	2.6×10^5	1562.	51	51
P128L0	128^3	0	2.1×10^6	781.3	107	107
P256L0	256^3	0	1.7×10^7	390.6	243	243
P064L3	64^3	3	5.6×10^5	195.3	67	493
P128L4	128^3	4	5.0×10^6	48.82	148	2259
P256L5	256^3	5	4.1×10^7	12.21	304	7281

4.2. Refinement strategy

The main ingredient in the cosmological simulations presented here is the refinement strategy. In order to increase the spatial resolution within collapsing regions, a quasi-Lagrangian mesh evolution was naturally chosen, using level dependent dark matter and gas density thresholds, as explained in Sect. 2.5. To be more specific, the level dependent density thresholds for the dark matter component were set to

$$\rho_\ell = 40\frac{\Omega_{\rm m} - \Omega_{\rm b}}{\Omega_{\rm m}}\frac{M_0}{(\Delta x^\ell)^3} \tag{38}$$

while for the baryonic component, they were set to

$$\rho_\ell = 40\frac{\Omega_{\rm b}}{\Omega_{\rm m}}\frac{M_0}{(\Delta x^\ell)^3}\cdot \tag{39}$$

In this way, a roughly constant number of particles per cell (between 5 and 40) is obtained, minimizing both collisionality and particle discreteness effects. Note that this number is higher than the pure dark matter simulations performed in Kravtsov et al. (1997), where 5 particles were used to trigger new refinements, instead of 40 in this paper. As explained above, this choice has basically two reasons: 1- we prefer to minimize as much as possible the effect of particle discreteness effect (Poisson noise) on fluid dynamics, 2- since the memory storage is dominated by fluid variables, we can increase the number of particles per cell by one order of magnitude for a given spatial resolution. The number 40 was finally retained to allow for a simple comparison with the more standard refinement threshold of Kravtsov et al. (1997), namely a factor of 2 decrease in spatial resolution.

Shock refinements, as discussed above, was not retained for these cosmological simulations. This choice has two reasons. First, the memory overhead associated to shock refinements would have been very large, since shock fronts occur everywhere in the hierarchical clustering picture. Since shock front are essentially two-dimensional, the number of cells required to cover the shock surfaces would have been completely out of reach, even for modern computers. Secondly, refining the mesh in low density regions where shock waves eventually propagate would violate the non-collisionality condition for dark matter dynamics. On the other hand, the AMR dynamics of shock fronts in this case (no shock refinements) was carefully investigated in the last sections. It turned out that as soon as shock waves

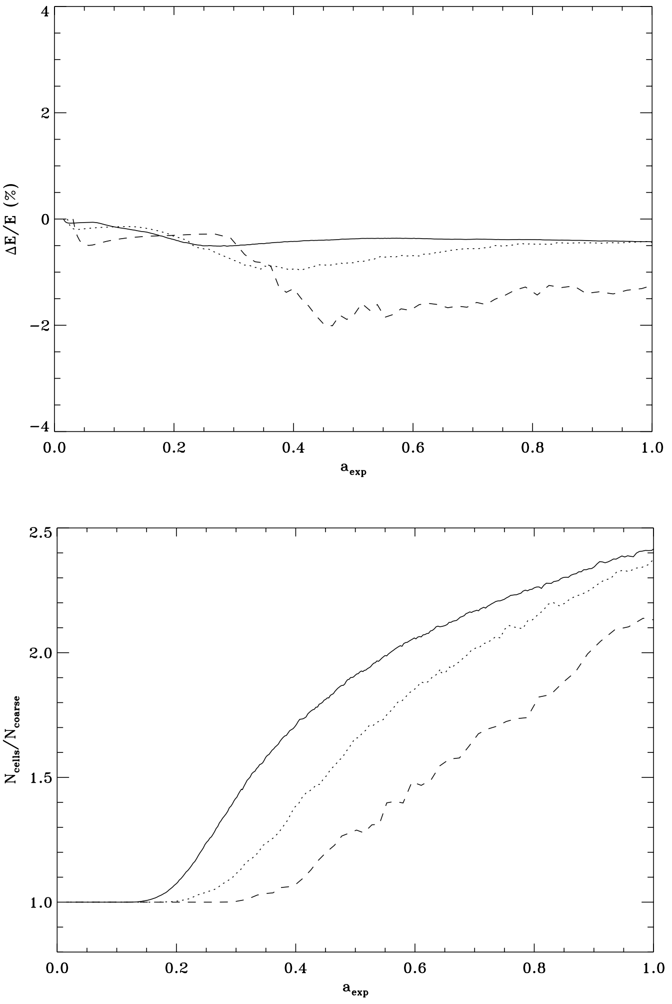

Fig. 9. Top: energy conservation as a function of expansion factor for run P256L5 (solid line), P128L4 (dotted line) and P064L3 (dashed line). Bottom: total number of cells in the AMR grid hierarchy (including split cells) divided by the initial number of coarse cells as a function of expansion factor for the same 3 runs.

travels from high-resolution to low-resolution regions, no spurious effects occurs. This last conditions turns out to be satisfied in cosmological simulations, as discussed in the next section.

The 3 different initial particle grids considered here (64^3, 128^3 and 256^3) defines also the coarse level ($\ell = 0$) of the AMR hierarchy in each run. The maximum level of refinement was set to 3, 4 and 5 respectively. This corresponds to a formal resolution of 512^3, 2048^3 and 8192^3 in the highest resolution regions. The corresponding spatial resolution is 195, 48 and 12 h^{-1} kpc. In all cases, adaptive time stepping was activated, with the following time step control parameters $C_1 = C_2 = cfl = 0.5$. In order to measure the advantage of adaptive mesh in cosmological simulations, these 3 runs were also performed without refinement ($\ell_{\max} = 0$).

4.3. Energy conservation and adaptive mesh evolution

A standard measure of the quality of a numerical simulation is to check for total energy conservation errors. Since Euler equations are solved in conservative form in RAMSES, the main source of energy conservation errors comes from the gravitational source terms, for both baryons and dark matter components. Figure 9 shows the total energy conservation (in the form of the Layzer-Irvine conservation equation for an expanding universe) for the 3 AMR runs. The maximum errors are found to be 2%, 1% and 0.5% for P064L3, P128L4 and P256L5 respectively. The maximum error in the energy conservation occurs when a significant number of refinements are built for the first time, around $1 + z \simeq 2$, 3 and 5 for P064L3, P128L4 and P256L5 respectively.

In Fig. 9 is also shown the total number of cells in the AMR tree structure (including split cells), in units of the number of coarse cells. It is worth noticing that this numbers should have remained exactly equal to 1 for a strict Lagrangian mesh like the ones described in Gnedin (1995) and Pen (1995). At the end of the simulations, as clustering develops, the final number of mesh points has increased by a factor of 2.5. This overhead is related to the mesh smoothing operator (see Sect. 2.1.1). The mesh evolution is therefore only "quasi" Lagrangian.

4.4. Adaptive mesh structure

The adaptive mesh is dynamically modified at each time step during the course of the simulation. Both hydrodynamics and N-body solvers take advantage of the increased spatial resolution to improve the accuracy of the solution in the refined regions.

Figure 10 illustrates this by comparing the gas and dark matter density fields in a slice cutting through the computational volume for run P256L5 (256^3 particles with 5 levels of refinements) with the density fields in the same slice for run P256L0 (same initial conditions without refinements). Only overdense cells are shown ($\rho > \Omega_b \rho_c$ for baryons and $\rho > (\Omega_m - \Omega_b)\rho_c$ for dark matter). One clearly sees that both gas and dark matter density fields are much more dense and clumpy when refinements are activated. On the other hand, it is reassuring to see that both simulations agree with each other on large scale.

The corresponding mesh structure is shown in the upper right part of Fig. 10. The interest of using a tree-based approach for defining the AMR hierarchy is striking: the grid structure closely follows the geometry of the density field, from a typical filamentary shape at large scale, to a more spherical and compact shape in the higher density haloes cores. If one examines the central filament connecting the 2 massive haloes in the images of Fig. 10, one sees that it follows a typical pancake-like structure, with 2 dark matter caustics on each side of a gas filament. This structure, though interesting, is not dense enough to be refined by our refinement strategy. We could have lowered the density thresholds to trigger new refinements in this

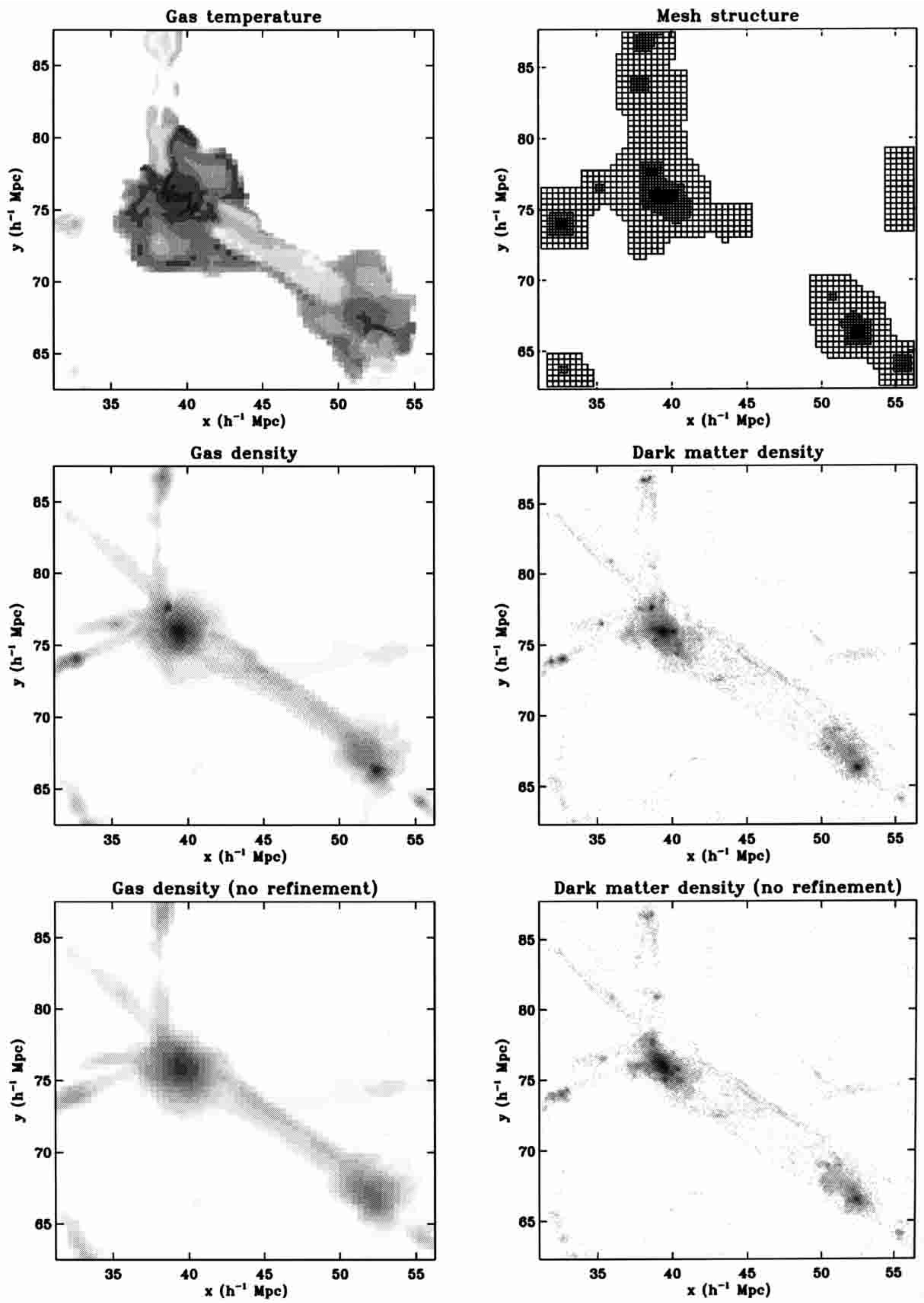

Gas temperature

Mesh structure

Gas density

Dark matter density

Gas density (no refinement)

Dark matter density (no refinement)

Fig. 10. Gray scale images of the gas temperature ($T > 10^5$ K), the gas density ($\rho > \Omega_{\rm b}\rho_{\rm c}$) and the dark matter density ($\rho > \Omega_{\rm m}\rho_{\rm c}$) in a planar cut through the computational volume for run P256L5. The mesh structure within the plane is plotted in the upper right panel (only octs boundaries are shown for visibility). For sake of comparison, the density and temperature maps obtained for run P256L0 (same initial conditions without refinements) are shown in the 2 lower panels.

region, at the price of an increased collisionality for dark matter. This would result in a spurious fragmentation of the pancake structure (Melott et al. 1997).

The temperature map ($T > 10^5$ K) in the same planar cut exhibits the typical flower-like structure of strong cosmological accretion shocks around large haloes. These strong shocks propagates exclusively in large voids in between filaments that intersect each other at the central halo position: this is due to the higher gas pressure within the filaments that inhibits shock propagation in the direction aligned with the filaments. This property of cosmological shock waves is of great importance here, since it implies that strong shocks propagates almost exclusively from high to low resolution regions of the grid. On the other hand, weak shocks occurring during sub-halo mergers along the filaments can enter high resolution regions of the mesh as clustering develops. Since the oscillatory behavior outlined in Sect. 3.5 disappears completely for weak shocks (Berger & Collela 1989; Khokhlov 1998), we can conclude that cosmological shocks propagation remains free from spurious effects associated to the adaptive mesh structure.

4.5. The halo model

In order to analyze the results of the simulations in a more quantitative way, I will use a powerful analytical theory: the so called *halo model*. Several authors (Seljak 2000; Ma & Fry 2000; Scoccimarro et al. 2001; Cooray et al. 2000; Cooray 2001; Refregier & Teyssier 2001) have recently explored the idea that both dark matter and baryons distributions can be described by the sum of two contributions: (1) a collection of virialized, hydrostatic haloes with overdensity $\geq$200 and described by the Press & Schechter mass function and (2) a smooth background with overdensity $\leq$10 described by the linear theory of gravitational clustering. The purpose of this paper is not to improve upon earlier works on this halo model, but rather to use it as an analyzing tool for our simulations. Therefore, the basic ingredients of the halo model are only briefly recalled and will not be discussed in great details. From now on, we consider only results obtained at the final redshift $z = 0$. The redshift evolution of the halo model is discussed and compared to numerical simulations elsewhere (Refregier et al. 2000; Refregier & Teyssier 2001).

Haloes are defined as virialized clump of gas and dark matter, with total mass defined as the Virial mass

$$M_{\rm vir} = \frac{4\pi}{3}\Delta_{\rm c}\rho_{\rm c}r_{\rm vir}^3 \tag{40}$$

where the Virial *density contrast* $\Delta_{\rm c}$ is related to the Virial *overdensity* by $\Delta_{\rm c} = \Omega_{\rm m}\Delta$. For $\Omega_{\rm m} = 0.3$ and $z = 0$, one has $\Delta \simeq 334$ (Eke et al. 1998). The dark matter follows the Navarro et al. (NFW; Navarro et al. 1996) density profile

$$\rho = \frac{\rho_{\rm s}}{(r/r_{\rm s})(1+r/r_{\rm s})^2} \tag{41}$$

whose parameters are connected to the halo Virial mass by

$$M_{\rm vir} = 4\pi\rho_{\rm s}r_{\rm s}^3\left[\ln(1+c) - \frac{c}{1+c}\right]\cdot \tag{42}$$

The only remaining free parameter (apart from $M_{\rm vir}$) is the so called concentration parameter $c = r_{\rm vir}/r_{\rm s}$. This parameter exhibits a good correlation with halo mass in numerical simulations that can be fitted analytically to match the numerical results (Ma & Fry 2000). The final ingredient is to assume that the halo distribution is described by the Press & Schechter mass function (Press & Schechter 1974).

The total mass power spectrum can then computed as the sum of 2 components $P(k) = P_1(k) + P_2(k)$, where $P_1(k)$ is a non-linear term corresponding to the mass correlation within halos, and $P_2(k)$ is a linear term corresponding to the mass correlation between 2 halos. Both terms have relatively straightforward analytical expressions that are not recalled here (Seljak 2000; Ma & Fry 2000; Scoccimarro et al. 2001).

The gas distribution within halos is supposed to follow the isothermal hydrostatic equilibrium. The temperature remains constant within the halo Virial radius, and is taken equal to the halo Virial temperature

$$\frac{k_{\rm B}T_{\rm vir}}{\mu m_{\rm H}} = \frac{1}{2}\frac{GM_{\rm vir}}{r_{\rm vir}}\cdot \tag{43}$$

Note that temperature profiles determined in numerical simulations are neither isothermal nor equal to the Virial temperature. Therefore, the halo model can only be considered as a crude approximation, describing the gas distribution in a statistical sense only. Moreover, the temperature profiles observed in large X-ray clusters is more or less affected by cooling flows in the central regions. Including all physical ingredients that might affect the thermal structure in the core of virialized halos is beyond the scope of this paper. Only adiabatic hydrodynamics is considered here.

Solving the hydrostatic equilibrium equation in the isothermal case (using the NFW mass distribution) leads to the following gas density profile (Suto et al. 1998)

$$\rho = \rho_0{\rm e}^{-b}\left(1+r/r_{\rm s}\right)^{br_{\rm s}/r} \tag{44}$$

where the dimensionless parameter b is given by

$$b = \frac{\mu m_{\rm H}4\pi G\rho_{\rm s}r_{\rm s}^2}{k_{\rm B}T_{\rm vir}}\cdot \tag{45}$$

The central density ρ_0 is computed by specifying that the total baryons mass within the Virial radius is equal to $\Omega_{\rm b}/\Omega_{\rm m}M_{\rm vir}$.

In the next section, the gas pressure power spectrum is computed from RAMSES numerical simulations and compared to the halo model predictions. The pressure power spectrum is quite an interesting quantity in cosmology, since it is directly related to the Sunyaev-Zeldovich induced Cosmic Microwave Background anisotropies angular power spectrum (Sunyaev & Zeldovich 1980;

Rephaeli 1995). It can be computed within the halo model framework using the same two terms as for the total mass density power spectrum $P(k) = P_1(k) + P_2(k)$. Exact analytical expressions can be found in Cooray (2001) and Refregier & Teyssier (2001).

4.6. Power spectra

In this section, both dark matter density and gas pressure power spectra are computed and compared to the halo model predictions. In order to study the convergence properties of the numerical solution, results obtained with different mass and spatial resolutions are examined.

4.6.1. Computing the power spectra

Computing power spectra for simulations with such high dynamical range requires to go beyond traditional methods based on regular Cartesian meshes: recall that our highest resolution run has a formal resolution of 8192^3. We use instead a multi-grid method based on a hierarchy of nested cubic Cartesian grids (Jenkins et al. 1998; Kravtsov & Klypin 1999). Each level of the hierarchy corresponds to the code AMR levels (from $\ell = 0$ to $\ell_{\max}$) and covers the whole computational volume with ℓ^3 cubic grids of size n_x^3. At a given level, a dark matter density field is computed for each grid using CIC interpolation, and all grids are stacked together in a single, co-added density field. This density field is then Fourier analyzed using FFT technique. From the resulting power spectrum, only modes spanning the range $2^\ell \times [k_{\min}, k_{\max}]$ are kept as reliable estimations of the true power spectrum, with $k_{\min} = k_{\text{nynq}}/8$ and $k_{\max} = k_{\text{nynq}}/4$. The Nyquist frequency k_{nynq} depends on the size of the cubic grid, chosen here equal to the coarse grid size n_x^3, so that $k_{\text{nynq}} = n_x\pi/L$. At the 2 extreme spatial scales, we have however $k_{\min} = 2\pi/L$ (for $\ell = 0$) and $k_{\max} = 2^{\ell_{\max}} k_{\text{nynq}}$ (for $\ell = \ell_{\max}$). The maximum frequency considered in the present analysis corresponds therefore to the formal Nyquist frequency of each simulation $k_{\max} = \pi/\Delta x_{\min}$ (see Table 1). The same procedure is applied to the pressure field, except that CIC interpolation is no longer needed.

4.6.2. Results

The resulting power spectra are shown in Fig. 11 for the 3 runs with refinements (labeled "AMR") and without refinements (labeled "PM"). For comparison, the dark matter and pressure power spectra predicted by the halo model are plotted as solid lines.

The dark matter power spectrum shows a striking agreement with the halo model prediction, down to the formal resolution limit. Note that the halo model free parameters has been tuned in order to recover simulations results (Ma & Fry 2000). Results obtained here are therefore consistent with those obtained by other authors (Jenkins et al. 1998; Kravtsov & Klypin 1999), and can be considered as a powerful integrated test of the code. For each mass resolution, the power spectrum is plotted up to the formal Nyquist frequency. For AMR runs with refinements activated, the numerical power spectrum is dominated at high wave numbers by the Poisson noise due to particle discreteness effects (see the small increase of power around k_{nynq}). We can conclude that the numerical power spectrum has converged for each run, down to the limit imposed by the finite mass resolution, without being affected by the finite spatial resolution. For runs without refinements, the limited dynamical range has a noticeable effect on the resulting power spectrum at much larger scale: the spatial resolution is therefore a strong limiting factor in this case.

Let us now examine the gas pressure power spectrum (Fig. 11). The overall agreement of the numerical results with the halo model predictions is relatively good: the correct behavior is captured at all scales within a factor of 2 for our highest resolution run (P256L5). Note that the halo model has no free parameters for the gas distribution, as soon as the dark matter parameters are held fixed. At large scale, the numerical power spectrum appear to converge to the halo model predictions (run P128L4 and run P256L5 give exactly the same results). Note that a rather high mass resolution is needed for this convergence to occur ($>128^3$ particles), as opposed to the dark matter density power spectrum for which the correct large scale power is recovered even with 64^3 particles. At intermediate scales (around 1 h Mpc^{-1}), the halo model predictions slightly underestimate the pressure power spectrum. Since numerical results have also converged at these scales, this discrepancy might be due to the fact that intermediate density regions ($10 < \rho < 200$) are completely neglected in the halo model. These regions are believed to be composed of warm filaments, whose pressure obviously cannot be completely neglected.

At small scales, the situation remains quite unclear. On one hand, one clearly sees in Fig. 11 that an increased dynamical range has a dramatic effect on the resulting pressure power spectra. The power is much higher on small scales for AMR runs than for runs without refinements. On the other hand, for AMR runs, the convergence of the numerical results to the "true" solution is not as fast as that of the dark matter power spectrum. Some hints of convergence between run P128L4 and run P256L5 can be seen in Fig. 11. Indeed, without refinements (runs P64L0, P128L0 and P256L0), the cut off in the pressure power spectrum is directly proportional to the spatial resolution of the simulation. The same is true between runs P64L3 and P128L4, while for run P256L5, the effect of spatial resolution appears to weaken slightly. More interesting is the large discrepancy in slope at large k between the halo model and the solution obtained by run P256L5. As discussed in the next section, this is probably due to the assumption of isothermality in the halo model, which is ruled out by simulation results for individual halo temperature profiles.

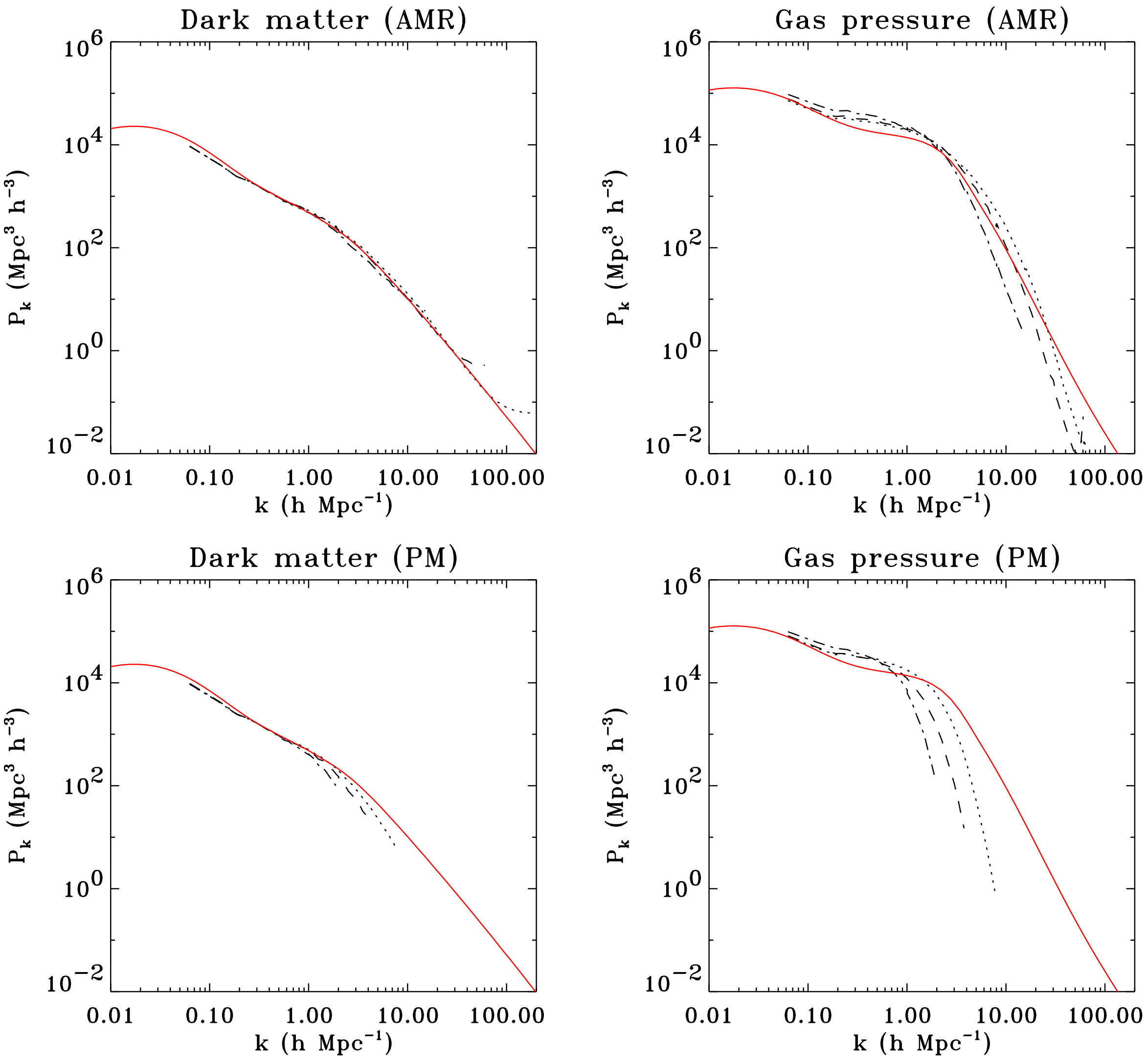

Fig. 11. Dark matter density (left panels) and gas pressure (right panels) power spectra for RAMSES runs with refinements (upper panels) and without refinements (lower panels). In each plot, the solid line corresponds to the halo model prediction, while the dotted line (dashed and dot-dashed) corresponds to numerical results with 256^3 (128^3 and 64^3) particles. Label "AMR" stands for AMR runs (P256L5, P128L4 and P64L3), while label "PM" stands for runs without refinement (P256L0, P128L0 and P64L0). For each power spectrum, the curve ends at the Nyquist frequency corresponding to the formal resolution of the simulation ($\Delta x_{\rm min}$ in Table 1).

4.7. Individual halos structure

The internal structure of the 5 largest halos found in the highest resolution run (P256L5) is now examined in great detail. It is worth mentioning that this analysis is made possible thanks to the large dynamical range obtained in our simulation ($\Delta x_{\rm min} = 12\ h^{-1}$ kpc), although it was not optimized to study individual halo properties. The next step to go beyond what is presented here would be to perform so called "zoom simulations", with nested, higher resolution, initial conditions particle grids centered on single halos (Bryan & Norman 1997; Eke et al. 1998; Yoshida et al. 2000; Abel et al. 2000). The main advantage of the present "brute force" approach is to combine both large and small scale results in the analysis. In order to study the convergence properties of individual halo profiles, results obtained for runs P256L5, P128L4 and P64L3 are compared. Recall that a direct comparison of the same halo at different mass and spatial resolution is possible, since the same initial conditions were used (and degraded to the correct mass resolution) for each run. Runs without refinement (P256L0, P128L0 and P64L0) are discarded from this analysis, because they completely lack the necessary dynamical range to resolve the internal structure of individual halos.

Haloes were detected in the dark matter particles distribution at the final output time ($z = 0$) using the Spherical Overdensity algorithm (Lacey & Cole 1993), with overdensity threshold $\Delta = 334$. Only the 5 most massive haloes of the resulting mass function are considered for the present analysis. Their global properties are listed in Table 2. For each halo, the center is defined as the location of the maximum in the dark matter density

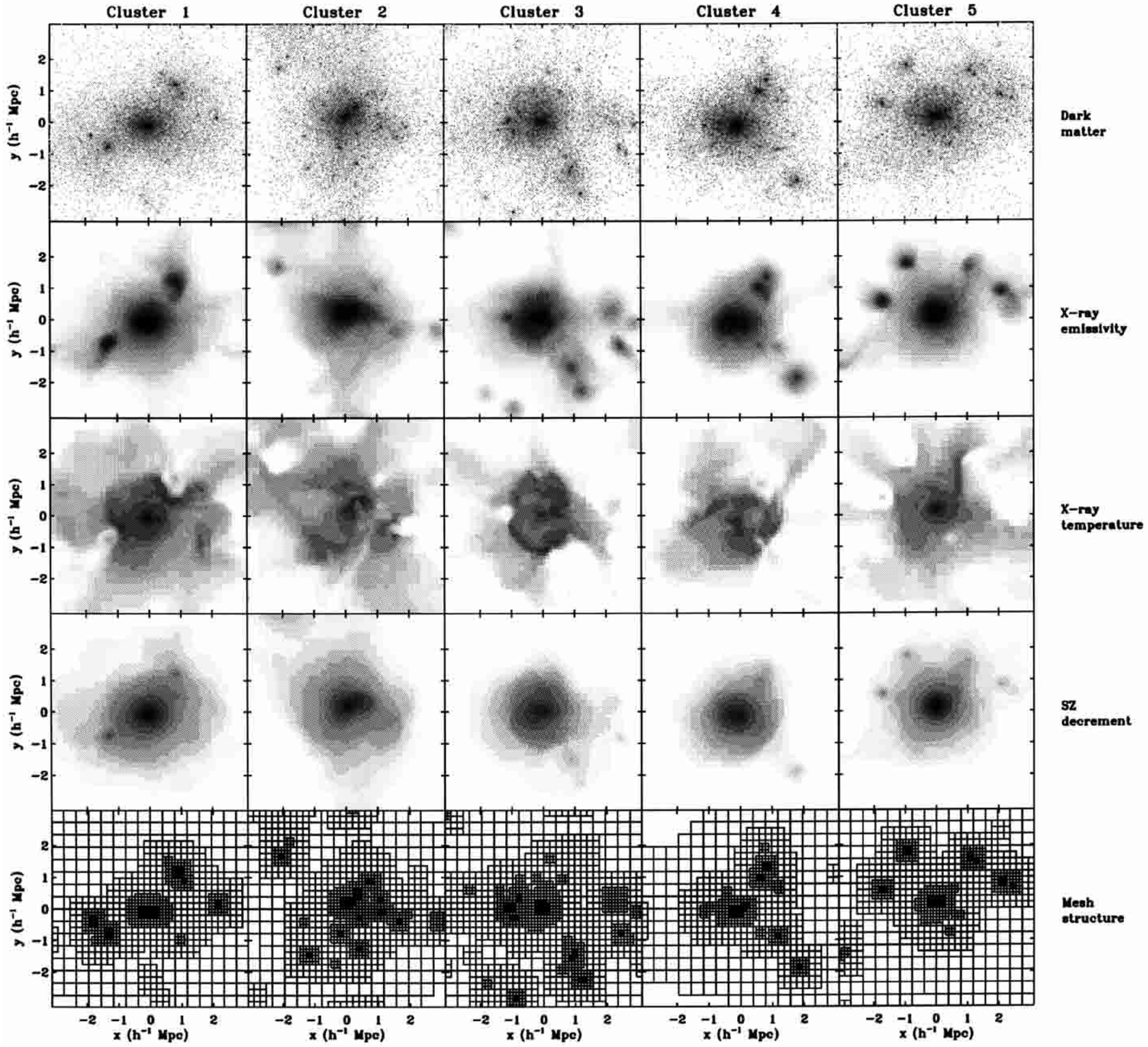

Fig. 12. Color maps showing various projected quantities for the 5 most massive halos extracted from run P256L5. The projected volume is in each case a cube of 6.25 h^{-1} Mpc aside. The color coding is based on a logarithmic scale for each plot. From top to bottom: 1- Projected dark matter particle distribution (the color coding corresponds to the local particle density). 2- X-ray emissivity map. 3- X-ray (emission weighted) temperature map. 4- Sunyaev-Zeldovich decrement parameter (equivalent to the integrated pressure along the line of sight). 5- Projected adaptive mesh structure (only oct boundaries are shown).

field. For regular, relaxed haloes, this definition also corresponds to the maximum in the baryons density field, and to the halo center of mass. This is however not the case for irregular, not yet relaxed haloes, for which this definition of the halo center is less robust.

Cubic regions 6.25 h^{-1} Mpc aside are then extracted around each halo center. The resulting projected color maps for various relevant quantities are shown in Fig. 12. Clusters 1 and 5 appear to be the most relaxed halos of our sample, while clusters 2, 3 and 4 show more substructures and irregularities within their Virial radii. The adaptive mesh structure, also shown in Fig. 12, closely matches the clumpy structure of each halo. Note that the maximum level of refinement ($\ell = 5$) is activated in the halo cores, where the formal spatial resolution reaches 12 h^{-1} kpc (barely visible in Fig. 12). The physical properties of these 5 haloes are now discussed quantitatively.

4.7.1. Dark matter distribution

The projected dark matter particles distribution is shown in Fig. 12, with a color coding corresponding to the local particle overdensity. The dark matter distribution is far from being smooth and spherically symmetric. It is

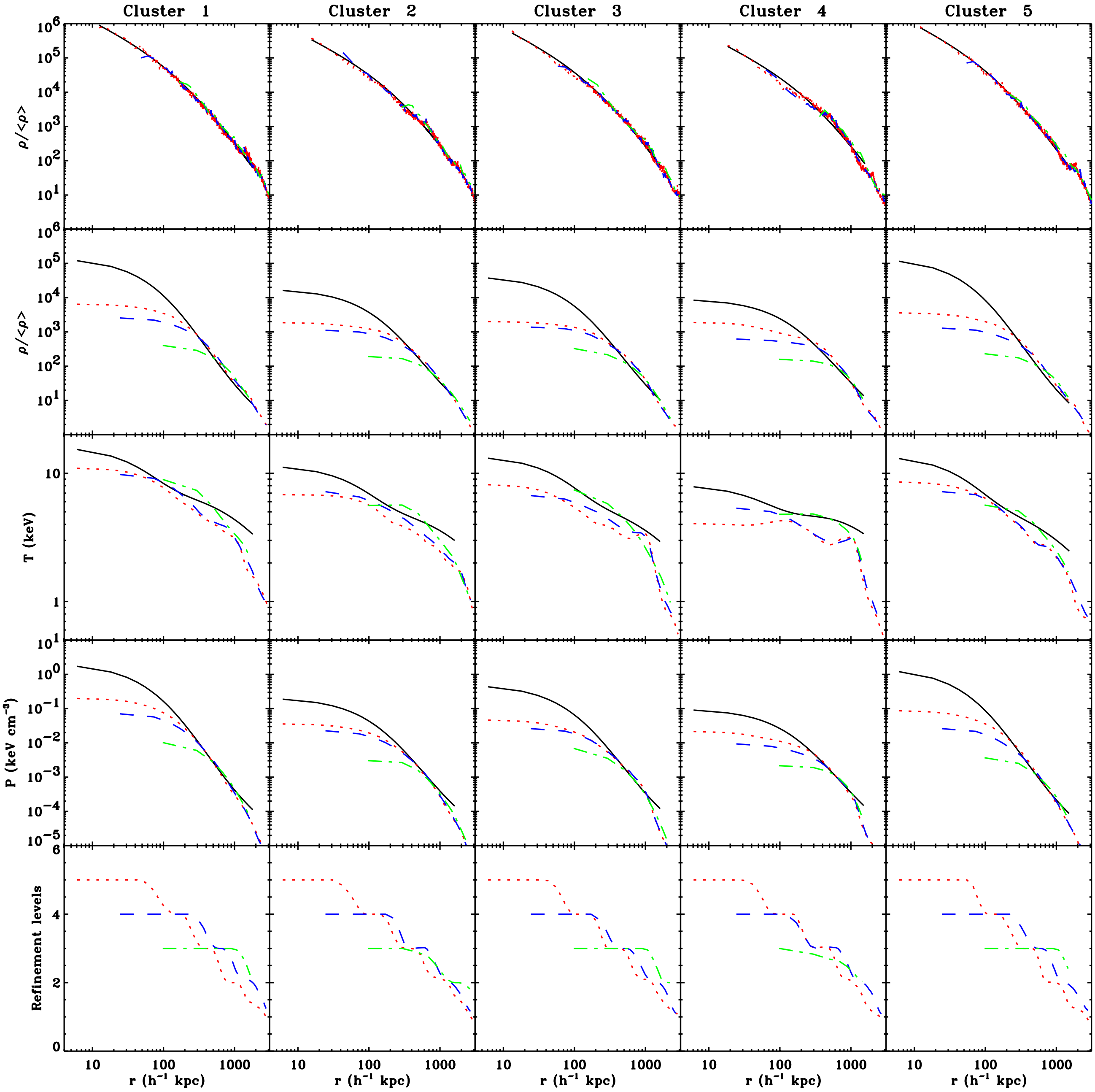

Fig. 13. Radial profiles for the 5 most massive halos showing various quantities averaged along radial bins. In each plot, the dotted line (dashed and dot-dashed) comes from run P256L5 (P128L4 and P64L3). From top to bottom: 1- Dark matter overdensity profile (the best-fit NFW analytical profile is shown as a solid line). 2- Gas overdensity profile (the corresponding "hydrostatic isothermal model" analytical profile is also shown as a solid line). 3- Mass averaged temperature profile (the corresponding "hydrostatic beta model" analytical profile is also shown as a solid line). 4- Pressure profile (the corresponding "hydrostatic isothermal model" analytical profile is also shown as a solid line). 5- Volume averaged refinement levels.

however interesting to compute the radial density profile and compare it to the NFW analytical prediction. The result is shown in Fig. 13, for our 3 different mass resolutions (runs P256L5, P128L4 and P64L3). The density profile obtained in the highest resolution run (P256L5) was fitted to the NFW profile, using the concentration parameter c as fitting parameter. Best fit values are listed in Table 2: they are fully consistent with expected values for a ΛCDM universe (Kravtsov et al. 1997; Eke et al. 1998).

The quality of the fit is impressive for clusters 1 and 5, which are also the more relaxed haloes of our sample. The poorest fit was obtained for cluster 4, with deviations as large as 50% at a radius of 150 h^{-1} kpc. A close examination of the corresponding map in Fig. 12 confirms that this halo is poorly relaxed in its central region. By comparing the profiles obtained for different mass resolution, one sees that the numerical profiles agree with each other down to their resolution limit. This is in complete agreement

Table 2. Global properties of the 5 largest halos extracted from the highest resolution run P256L5.

Name	$M_{\rm vir}$ $h^{-1}M_\odot$	$r_{\rm vir}$ h^{-1}Mpc	c	$\beta_{\rm fit}$	$r_{\rm core}$ h^{-1}kpc
Cluster 1	6.97×10^{14}	1.82	9.5	0.85	144.2
Cluster 2	5.09×10^{14}	1.64	5.9	0.80	215.5
Cluster 3	5.07×10^{14}	1.63	7.3	0.80	202.3
Cluster 4	4.52×10^{14}	1.57	4.9	0.64	147.0
Cluster 5	4.29×10^{14}	1.55	9.4	0.84	159.7

with our conclusion concerning the dark matter power spectrum: simulated power spectra match closely the halo model prediction down to their formal Nyquist frequency.

4.7.2. Baryons distributions

The baryons distribution within the selected haloes is similar on large scales to the dark matter distribution. In Fig. 12, simulated X-ray emission maps (using $L_X \propto n_e^2$) are good tracers of the gas overdensity projected along the line of sight. One can notice however that the hot gas is more smoothly distributed than dark matter. This is even more striking in the central region of all clusters, where the gas density reaches a plateau, reminiscent of a β model density profile. It is worth noticing that overdensities (substructures) in the gas distribution usually appears as cold spots in the X-ray (emission weighted) temperature map. On the other hand, the cluster cores are significantly hotter than the surrounding gas in most cases. We will come back to this point later.

Using the halo center as defined above, gas overdensity, mass weighted temperature and pressure profiles were computed as a function of radius and plotted in Fig. 13. For that purpose, conserved variables such as mass and internal energy are averaged into radial bins of increasing thickness, starting from the formal resolution (12 h^{-1} kpc for run P256L5) up 3 times this value at the Virial radius. The volume averaged refinement level is also plotted in Fig. 13, giving some hints of the effective spatial resolution as a function of radius. Based on the results obtained during the Spherical Secondary Infall test presented in Sect. 3.8, the actual resolution of the code corresponds roughly to twice its formal resolution. For run P256L5 (P128L4 and P64L3), this gives a limiting radius of 24 (96 and 384) h^{-1} kpc, above which numerical results are fully reliable.

Since dark matter density profile are well fitted for each halo by the NFW analytical profile, the corresponding gas density profile can be computed using Eq. (44). Recall that in the halo model, the gas temperature is assumed to remain constant within the Virial radius, and equal to the Virial temperature (Eq. (43)). This is obviously not the case for our simulated clusters (see Fig. 13), and explains why the halo model profile is much more peaked in the central region than for simulated profiles. For the pressure profiles, the situation is however less dramatic, though still unsatisfactory. It is interesting to notice that here again, the behavior of the pressure profiles is fully consistent with previous results concerning the pressure power spectrum: the isothermal halo model overestimates the pressure power on small scales. This translates in to a much steeper slope at low radii, as for the pressure power spectrum at large k. Moreover, numerical results for the gas distribution within haloes have clearly not converged yet, although the dependance of the computed profiles with respect to the spatial resolution seems to weaken slightly between run P128L4 and run P256L5, in exactly the same way as the pressure power spectrum did in Sect. 4.6.2. Conclusions are therefore similar: numerical results show good evidence of converging at scales greater than 50 h^{-1} kpc. Similar conclusions were obtained by Bryan & Norman (1997) for a "zoom" simulation of a single cluster. These authors obtained very similar gas density and temperature profiles, with quite the same convergence properties as the one obtained here. Consequently, the isothermal halo model is likely to fail at scales less than 250 h^{-1} kpc.

4.7.3. Beyond the isothermal halo model?

As noted by several authors (Bryan & Norman 1997; Eke et al. 1998), the typical gas density profile obtained in numerical simulations is much more accurately described by the β model analytical solution (Cavaliere & Fusco-Femiano 1976)

$$\rho = \rho_0 \left[1 + (r/r_{\rm core})^2\right]^{-3\beta_{\rm fit}/2}. \tag{46}$$

Although the numerical results presented here have not fully converged yet, it is worth exploring an alternative to the isothermal halo model. The gas overdensity profile obtained in run P256L5 was thus fitted with the β model formula, using both $r_{\rm core}$ and $\beta_{\rm fit}$ as fitting parameters. Best fit values are listed in Table 2 and are consistent with typical numbers quoted by other authors (e.g. Eke et al. 1998). It is worth mentioning that the quality of the fit is excellent in each case, except for cluster 4, as expected from the previous analysis on the dark matter distribution.

Since both gas and dark matter density profiles are now determined to a good accuracy, it is possible to perform a consistency check and compute the temperature profile resulting from the assumption of hydrostatic equilibrium. For that purpose, the analytical framework developed by Varnieres & Arnaud (2001) is exactly what is needed here: assuming a NFW profile for dark matter and a β model for baryons, they derived analytically the corresponding hydrostatic temperature profile. This temperature profile is shown for each cluster in Fig. 13. The agreement with numerical results is good: temperature rising towards the halo center is therefore a direct consequence of hydrostatic equilibrium. After closer examination, the small (20%) disagreement observed in clusters 2, 3 and 4 is due to the poorer fit of the NFW formula to the dark matter simulated density profiles.

This non constant behavior of the halo temperature profile have been already noticed by several authors in numerical simulations (Bryan & Norman 1997; Eke et al. 1998; Loken et al. 2000) and also in X-ray observations of large galaxy clusters (Markevitch et al. 1998). Note however that more physics need to be included in current numerical simulations before performing a reliable comparison to observations. On the other hand, the idealized case of adiabatic gas dynamics is still of great theoretical interest: one can hope to find a self-consistent description of the gas distribution within haloes using such an approach. The main ingredient to extend the halo model in this framework is to determine the typical core radius (as well as $\beta_{\rm fit}$) as a function of halo mass and redshift. Eke et al. (1998) have already initiated this challenging task using high resolution (zoom) SPH simulations for large mass haloes ($M \simeq 10^{15} h^{-1} M_\odot$), but more work need to be done to probe a larger mass and redshift range. Using the analytical formula of Varnieres & Arnaud (2001), it would be straightforward to determine the corresponding temperature profile, and thus to complete the description of the baryons component within this extended halo model. This ambitious project will not be addressed here, but will be considered in a near future.

5. Conclusions and future projects

A new N-body/hydrodynamical code, RAMSES, has been presented and tested in various configurations. RAMSES has been written in FORTRAN 90 and optimized on a vectorized hardware, namely the Fujitsu VPP 5000 at CEA Grenoble. A parallel version was also impemented on shared-memory systems using OpenMP directives. A distibuted memory version of RAMSES is currently under construction using a domain decomposition approach.

The main features of the RAMSES code are the followings:

1- the AMR grid is built on a tree structure, with new refinements dynamically created (or destroyed) on a cell-by-cell basis. This allows greater flexibility to match complicated flow geometries. This property appears to be especially relevant to cosmological simulations, since clumpy structures form and collapse everywhere within the hierarchical clustering scenario;

2- the hydrodynamical solver is based on a second order Godunov method, a modern shock capturing method that ensures exact total energy conservation, as soon as gravity is not included. Moreover, shock capturing relies on a Riemann solver, without any artificial viscosity;

3- the refinement strategy that was retained for cosmological simulations is based on a "quasi-Lagrangian" mesh evolution. In this way, the number of dark matter particles per cell remains roughly constant, minimizing two-body relaxation and Poisson noise. On the other hand, this refinement strategy is not optimal for baryons, since one neglects to refine shock fronts (this would have been too costly anyway). It has been carefully shown that in this case, as soon as strong shocks propagate from high to low resolution regions of the grid, no spurious effects appear.

The code has been tested in standard gas dynamical test cases (Sod's test and Sedov's test), but also for integrated cosmological tests, like Zel'dovich pancake collapse or Bertschinger spherical secondary infall. It has been shown that the actual resolution limit of the code is equal to roughly twice the cell size of the maximum refinement level.

The RAMSES code has been finally used to study the formation of structures in a low-density ΛCDM universe. A careful convergence analysis has been performed, using the same initial conditions with various mass and spatial resolutions, for a fixed box size $L = 100\ h^{-1}$ Mpc. The initial number of cell (at the coarse level) was set equal to the initial particle grid (64^3, 128^3 or 256^3), for a final number of cells only 2.5 larger. The formal spatial resolution in the largest run was 8192^3 or 12 h^{-1} kpc comoving.

Numerical results have been compared to the analytical predictions of the so called halo model, for both dark matter and gas pressure power spectra, as well as individual haloes internal structure. A good agreement was found between the halo model and the numerical results for dark matter, down to the formal resolution limit. For the baryons distribution, numerical results show some evidence of converging at scales greater than 50 h^{-1} kpc for our highest resolution run. The halo model reproduces simulations results only approximatively (within a factor of 2) at these scales.

A simple extension of the halo model for the fluid component has been proposed. The idea is to assume that the average gas density profile within haloes is described by a β model, whose parameters still need to be determined from first principles or from numerical simulations and for a rather large mass range, which is far beyond the scope of this paper (see however Eke et al. 1998). It is then possible to deduce from hydrostatic equilibrium an analytical temperature profile (Varnieres & Arnaud 2001) that accurately matches the simulation results presented in this paper, and should therefore improve considerably the halo model.

Extending the current work to "zoom" simulations is currently under investigation, using a set of nested grids as initial conditions, in order to improve mass and spatial resolutions inside individual haloes. This approach seems indeed very natural within the AMR framework, and has already proven to be successful in recent attempts (Bryan & Norman 1997; Abel et al. 2000). Future efforts in the RAMSES code development will be however more focused on including more physics in the description of the gaseous component, like cooling, star formation and supernovae feedback.

Acknowledgements. The simulations presented in this paper were performed on the Fujitsu VPP 5000 system of the Commissariat à l'Energie Atomique (Grenoble). I would like to thank Philippe Kloos for his help on optimizing the code. I would like to thank Remy Abgrall for inviting me to the

CEMRACS Summer School 2000 in Luminy (Marseille), where part of this work was initiated. Special thanks to Alexandre Refregier who has provided me with the software to compute analytical power spectra predicted by the halo model, and to Stéphane Colombi who has provided me with the software to compute numerical power spectra. I would like to thank Jean-Michel Alimi, Edouard Audit, François Bouchet and Jean-Pierre Chièze for enlightening discussions about the numerical methods discussed in this paper. The author is grateful to an anonymous referee, whose comments greatly improved the quality of the paper.

References

Abel, T., Bryan, G. L., & Norman, M. L. 2000, ApJ, 540, 39
Almgren, A. S., Bell, J. B., Colella, P., Howell, L. H., & Welcome, M. L. 1998, J. Chem. Phys., 142, 1
Barnes, J., & Hut, P. 1986, Nature, 324, 446
Berger, M. J., & Collela, P. 1989, J. Chem. Phys., 82, 64
Berger, M. J., & Oliger, J. 1984, J. Chem. Phys., 53, 484
Bertschinger, E. 1985, ApJS, 58, 39
Bouchet, F. R., & Hernquist, L. 1988, ApJS, 68, 521
Bryan, G. L., & Norman, M. L. 1997, in ASP Conf. Ser. 123, Computational Astrophysics; 12th Kingston Meeting on Theoretical Astrophysics, pp. 363–364
Cavaliere, A., & Fusco-Femiano, R. 1976, A&A, 49, 137
Cen, R. 1992, ApJS, 78, 341
Chieze, J., Alimi, J., & Teyssier, R. 1998, ApJ, 495, 630
Collela, P. 1990, J. Chem. Phys., 87, 171
Collela, P., & Woodward, P. R. 1984, J. Chem. Phys., 54, 174
Cooray, A. 2001, Phys. Rev. D, in press [`astro-ph/0005287`]
Cooray, A., Hu, W., & Miralda-Escudé, J. 2000, ApJ, 535, L9
Couchman, H. M. P. 1991, ApJ, 368, L23
De Zeeuw, D. L. 1993, Ph.D. Thesis, University of Michigan
Efstathiou, G., Davis, M., White, S. D. M., & Frenk, C. S. 1985, ApJS, 57, 241
Eke, V. R., Navarro, J. F., & Frenk, C. S. 1998, ApJ, 503, 569
Evrard, A. E. 1988, MNRAS, 235, 911
Fryxell, B., Olson, K., Ricker, P., et al. 2000, ApJS, 131, 273
Gingold, R. A., & Monaghan, J. J. 1977, MNRAS, 181, 375
Gnedin, N. Y. 1995, ApJS, 97, 231
Gnedin, N. Y., & Bertschinger, E. 1996, ApJ, 470, 115
Hernquist, L., & Katz, N. 1989, ApJS, 70, 419
Hockney, R. W., & Eastwood, J. W. 1981, Computer Simulation Using Particles, Computer Simulation Using Particles (New York: McGraw-Hill)
Jenkins, A., Frenk, C. S., Pearce, F. R., et al. 1998, ApJ, 499, 20
Jessop, C., Duncan, M., & Chau, W. Y. 1994, J. Chem. Phys., 115, 339
Khokhlov, A. M. 1998, J. Chem. Phys., 143, 519
Klypin, A. A., & Shandarin, S. F. 1983, MNRAS, 204, 891
Knebe, A., Kravtsov, A. V., Gottlöber, S., & Klypin, A. A. 2000, MNRAS, 317, 630
Kravtsov, A. V., & Klypin, A. A. 1999, ApJ, 520, 437
Kravtsov, A. V., Klypin, A. A., & Khokhlov, A. M. 1997, ApJS, 111, 73
Lacey, C., & Cole, S. 1993, MNRAS, 262, 627
Loken, C., Norman, M., Nelson, E., et al. 2000, in American Astronomical Society Meeting, 197, 10721
Ma, C. 1998, ApJ, 508, L5
Ma, C., & Fry, J. N. 2000, ApJ, 543, 503
Markevitch, M., Forman, W. R., Sarazin, C. L., & Vikhlinin, A. 1998, ApJ, 503, 77
Martel, H., & Shapiro, P. R. 1998, MNRAS, 297, 467
Melott, A. L., Shandarin, S. F., Splinter, R. J., & Suto, Y. 1997, ApJ, 479, L79
Navarro, J. F., Frenk, C. S., & White, S. D. M. 1996, ApJ, 462, 563
Pen, U. 1995, ApJS, 100, 269
Press, W. H., & Schechter, P. 1974, ApJ, 187, 425
Press, W. H., Teukolsky, S. A., Vetterling, W. T., & Flannery, B. P. 1992, Numerical recipes in FORTRAN. The art of scientific computing (Cambridge: University Press), 2nd ed.
Refregier, A., Komatsu, E., Spergel, D. N., & Pen, U. L. 2000, Phys. Rev. D, 61, 123001
Refregier, A., & Teyssier, R. 2001, A&A, submitted [`astro-ph/0012086`]
Rephaeli, Y. 1995, ARA&A, 33, 541
Ryu, D., Ostriker, J. P., Kang, H., & Cen, R. 1993, ApJ, 414, 1
Saltzman, J. S. 1994, J. Chem. Phys., 115, 153
Scoccimarro, R., Sheth, R. K., Hui, L., & Jain, B. 2001, ApJ, 546, 20
Sedov, L. I. 1993, Similarity and Dimensional Methods in Mechanics (Boca Raton: CRC Press), 10th ed.
Seljak, U. 2000, MNRAS, 318, 203
Sunyaev, R. A., & Zeldovich, I. B. 1980, ARA&A, 18, 537
Suto, Y., Sasaki, S., & Makino, N. 1998, ApJ, 509, 544
Teyssier, R., Chièze, J., & Alimi, J. 1998, ApJ, 509, 62
Toro, E. F. 1997, Riemann Solvers and Numerical Methods for Fluid Dynamics (Berlin: Springer)
Truelove, J. K., Klein, R. I., McKee, C. F., et al. 1998, ApJ, 495, 821
Varnieres, P., & Arnaud, M. 2001, in preparation
White, M., & Bunn, E. F. 1995, ApJ, 450, 477
Yahagi, H., & Yoshii, Y. 2001, ApJ, 558, 463
Yoshida, N., Springel, V., White, S. D. M., & Tormen, G. 2000, ApJ, 535, L103